Monthly Notices
of the
ROYAL ASTRONOMICAL SOCIETY

MNRAS **481,** 727–748 (2018)
Advance Access publication 2018 August 9

doi:10.1093/mnras/sty2188

Impact of Laser Guide Star facilities on neighbouring telescopes: the case of GTC, TMT, VLT, and ELT lasers and the Cherenkov Telescope Array

M. Gaug [1]★ and M. Doro [2]

[1] *Unitat de Física de les Radiacions, Departament de Física, and CERES-IEEC, Universitat Autònoma de Barcelona, E-08193 Bellaterra, Spain*
[2] *Department of Physics and Astronomy (DFA) of the University of Padova and INFN Padova, I-35131 Padova, Italy*

Accepted 2018 August 4. Received 2018 August 3; in original form 2018 June 24

ABSTRACT

Powerful Laser Guide Star (LGS) systems are standard for the next generation of extremely large telescopes. However, modern earth-based astronomy has gone through a process of concentration on few sites with exceptional sky quality, resulting in those becoming more and more crowded. The future LGS systems encounter hence an environment of surrounding astronomical installations, some of which observing with large fields of view. We derive formulae to calculate the impact of LGS light on the camera of a neighbouring telescope and the probabilities for a laser crossing the camera field of view to occur, and apply these to the specific case of the next very high energy gamma-ray observatory 'Cherenkov Telescope Array' (CTA). Its southern part shall be constructed in a valley of the Cerro Armazones, Chile, close to the 'Very Large Telescope' and the 'European Extremely Large Telescope' (ELT), while its northern part will be located at the 'Observatorio del Roque de los Muchachos', on the Canary Island of La Palma, which also hosts the 'Gran Telescopio de Canarias' (GTC) and serves as an optional site for the 'Thirty Meter Telescope' (TMT), both employing LGS systems. Although finding the artificial star in the field of view of a CTA telescope will not disturb observations considerably, the laser beam crossing the field of view of a CTA telescope may be critical. We find no conflict expected for the ELT lasers, however, 1 per cent (3 per cent) of extra-galactic and 1 per cent (5 per cent) of galactic observations with the CTA may be affected by the GTC (TMT) LGS lasers, unless an enhanced version of a laser tracking control system gets implemented.

Key words: atmospheric effects – instrumentation: adaptive optics – site testing – telescopes – gamma-rays: general.

1 INTRODUCTION

Laser Guide Star (LGS) systems (Bonaccini Calia et al. 2010, 2014; d'Orgeville & Fetzer 2016) provide artificial reference sources to partially correct the impact of atmospheric turbulence on astronomical observations. They are used in coincidence with Adaptive Optics (AO) systems. LGSs are used to provide increased sky coverage and availability compared to natural guide stars (Foy & Labeyrie 1985).

Mostly, high-power lasers tuned to the D_{2a} resonance of sodium atoms (at 589.159 nm in vacuum) are propagated at a sky location within the field of view of the optical telescope for which the wavefront needs correction. High-power sodium lasers produce artificial stars by exciting a layer of sodium atoms from their $3S_{1/2}$ to the $3P_{3/2}$ level in the mesosphere which produce fluorescence emission while de-exciting. The emission is centred at an altitude of (91.9 ± 0.8) km a.s.l. and has an equivalent full width at half-maximum of $\sim(11.3 \pm 1.2)$ km (Moussaoui et al. 2010).

The used laser light is often circularly polarized to achieve maximum impact (Boyer, Ellerbroek & Gilles 2010; Holzlöhner et al. 2010). The creation of several guide stars is also possible, to achieve asterism with a radial distance from science target ranging from 0.5 to 6 arcmin on the sky. The LGS will likely be operated regularly during observations, and their scattered light (Rayleigh and Mie) will then be seen by other telescopes until distances of several kilometres from the location of their host observatory.

Assuming the close-by installation observes in a wavelength range enclosing that of the LGS lasers, the scattered laser light may then leave spurious light tracks on the cameras and affect operation in several ways: (a) by generating false triggers (for installations that trigger

★ E-mail: markus.gaug@uab.cat

image readout, e.g. from Cherenkov light pulses), (b) the star guider camera and the precision pointing of the telescopes, and ultimately, (c) by affecting the duty cycle, if active laser avoidance is chosen. Several of the enumerated problems can be often overcome with the use of Notch filters (Schallenberg et al. 2010) or band-pass filters (Ahnen et al. 2017; Archambault et al. 2017), however this is not always possible at a reasonable cost, particularly not in the case of the CTA, where every camera pixel would need to be covered by such a filter. Light losses at smaller wavelengths, particularly in the sensitive region from 300 to 500 nm, need to be strictly controlled in order to ensure that sensitivity losses remain acceptable, particularly around the energy threshold of the CTA. It is therefore important to compute the amount of light that can reach a neighbouring installation, as well as to discuss the probability of interferences. The latter depends on the angular separation between the direction of the lasers and the telescopes' optical axis, the distance to the crossing point and its altitude, the size of the collecting surface of the telescopes, and the photon detection efficiency (PDE) of the photosensors.

The goal of this study is to provide a reference formalism to address this two-fold interference (spurious light yield and probability of crossings). This is done through the paper with a general approach, but is quantified for the particular case of the oncoming Cherenkov Telescope Array (CTA).

CTA (Actis et al. 2011) will be an observatory for gamma-ray astronomy in the GeV–TeV energy range. It is based on the so-called Imaging Atmospheric Cherenkov Technique (IACT) that captures the Cherenkov light emitted by extensive air showers (EASs), produced when very high energy gamma-rays hit the Earth's atmosphere. The EAS is a cascade of a large number of sub-atomic particles (mainly electrons and positrons) which reaches a maximum at altitudes between 8 and 12km a.s.l. for a 1 TeV shower, on average, however, moving to considerably higher altitudes at lower energies. The relativistic particles forming the cascade emit Cherenkov light that propagates towards the ground. The Cherenkov light emission is strongest in the ultraviolet and blue, hence the CTA telescopes and cameras are optimized to a wavelength range from 300 to 500 nm, but are also sensitive in the green, and even yellow, part of the optical spectrum. Silicon-photomultiplier-based cameras may even extend sensitivity beyond 900 nm (Otte et al. 2017).

CTA will operate at two sites: one in the Northern hemisphere, at the Observatorio del Roque de los Muchachos (ORM), La Palma, Spain, and one in the Southern hemisphere, at a Chilean site of the European Southern Observatory (ESO), close to Paranal. The northern array (hereafter CTA-N) has been formally accepted, and construction has already started. Negotiations about the southern array (hereafter CTA-S) are close to being concluded with the Chilean authorities and the ESO. Both arrays will consist of several telescopes of different sizes: four large-sized telescopes (LSTs) of 23 m diameter mirror dish each, in the central core of the array, 15 medium-sized telescopes (MSTs) of a 12 m diameter mirror in CTA-N, and 25 MSTs in CTA-S surrounding the LSTs, while CTA-S will be additionally equipped with 70 small-sized telescopes (SSTs) of an equivalent mirror diameter of about 4 m.[1] In the southern array, telescopes will be installed across a large area of roughly 2.2 × 2.4 km, centred at 24.674° S, 70.316° W, at 2150 m a.s.l. At a distance of about 10 km in the NW direction from the centre of CTA-S, the Very Large Telescope (VLT)[2] is taking data since 1998. Slightly further away, in the NE direction, at 15.8 km, the European Extremely Large Telescope (ELT)[3] is under construction. The northern array is somewhat smaller, covering an area of about 500 × 600 m, between the current ORM residence and the higher altitude rim of the Caldera de Taburiente Mountain, which hosts several optical telescopes. In between, the Gran Telescopio de Canarias (GTC),[4] located at 28.762° N, 17.892° W, is found, at about 550 m from the centre of the CTA-N. Further in that direction, at a distance of 1150 m from the centre of the CTA-N and located at 28.753° N, 17.897° W, the Thirty Meter Telescope (TMT)[5] may be installed, if finally the ORM is chosen to host it. Because the MST and SST telescopes are widely distributed around the central LSTs, several of them will in some cases further approach the VLT or ELT (at the CTA-S), or the GTC or TMT (at the CTA-N). See Fig. 1 for a schematic view of both sites and their neighbouring installations. The four above-mentioned telescopes VLT, ELT, GTC, and TMT, incorporate or will incorporate Laser Guide Star Facilities (LGSFs) that contain powerful continuous wave lasers (Ageorges & Hubin 2000; Wei et al. 2012; Herriot et al. 2014) to create artificial guide stars for the AO system of their primary mirrors: one in the case of the GTC, four in the case of VLT, and up to six in the case of the extremely large telescopes ELT and TMT. The TMT plans to create some asterism such that the outermost LGS will be distributed along circles with a perimeter of typically between 35 and 70 arcsec (Boyer et al. 2010).[6] Each AO-laser itself is extremely well collimated [$\simeq O$ (arcsec)] and operates at the vacuum wavelength of $\lambda_{\rm lgs} = 589.159$ nm, with a typical exit power of the order of ∼20 W, after exiting the beam transfer optics. Systems operating pulsed lasers in the UV (355 nm; Tokovinin et al. 2016) and in green (515 or 532 nm; Rutten et al. 2006; Rabien et al. 2011) have been built as well, but are not a primary option for the extremely large telescopes. The LGS lasers will operate till elevations of as low as 20° and could therefore cross the view-cone of some of the telescopes of the CTA.

The paper is structured as follows. In Section 2, we compute the amount of LGS induced light on a generic camera receiver unit pixel at the position of a putative neighbouring instrument. In Section 3, we estimate the probabilities that the LGS laser light beams cross the field of view of a neighbouring instrument and impede re-positioning. In Section 4, we quantify the two effects for the realistic case of CTA

[1] See also https://www.cta-observatory.org.
[2] www.eso.org/public/teles-instr/paranal-observatory/vlt/
[3] https://www.eso.org/sci/facilities/eelt/
[4] http://www.gtc.iac.es/
[5] https://www.tmt.org/
[6] Larger asterisms reaching up to 510 arcsec in perimeter have been presented in Boyer et al. (2010), but require more than six LGSs, which are currently not foreseen.

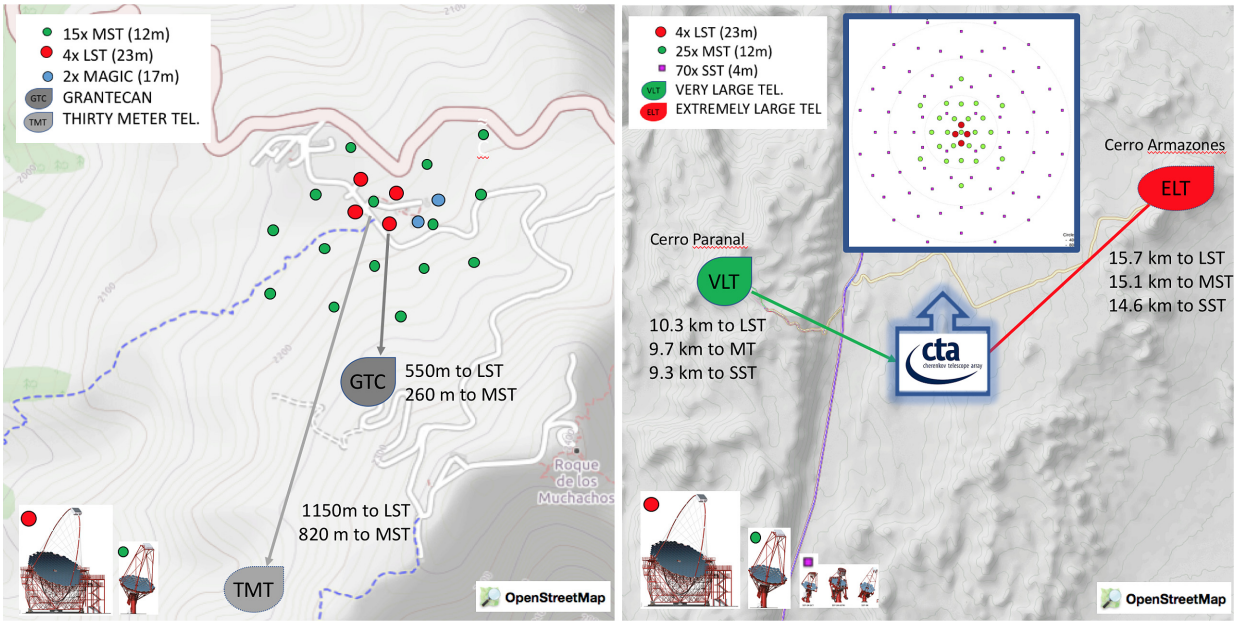

Figure 1. A schematic view of the Northern hemisphere site of CTA (CTA-N, left) at the *Observatorio del Roque de Los Muchachos* on the Canary Island of La Palma, Spain, and of the Southern CTA Site (CTA-S, right) at the ESO site of *Cerro Armazones*, Chile. The planned disposition of CTA telescopes is shown, together with the locations of the existing VLT and GTC telescopes, the ELT under construction as well as the possible location of the TMT. Distances from the optical telescopes to the closest CTA telescopes are marked. The underground map has been obtained with `openstreetmap.org` and the CTA layout from `www.cta-observatory.org`.

Table 1. Characteristics of the AO laser systems of the GTC, TMT, VLT, and ELT telescopes and distances compared to CTA telescopes.

Parameter	Value (GTC)	Value (TMT)	Value (ELT)	Value (VLT)	Comments
Number of lasers	1	6	6	4	–
DC power	16.5 W	6 × 16.5 W	6 × 16.5 W	4 × 17 W	22 W laser, assuming 75 per cent Beam Transfer Optics and Laser Launch Telescopes throughput (Bonaccini Calia et al. 2010), 88 per cent for VLT (Bonaccini Calia et al. 2014)
Vacuum wavelength	589.159 nm	589.159 nm	589.159 nm	589.159 nm	minor admixtures of 589.157 and 589.611 nm (Vogt et al. 2017)
Operation elevation	30°–90°	25°–90°	20°–90°	–	–
Duty Cycle AO-laser	15 per cent	$\gtrsim$75 per cent	∼50 per cent	–	–
Latitude	28°45′23.8″ N	28°45′09″ N	24°35′21″ S	24°37′38″ S	–
Longitude	17°53′30.8″ W	17°53′45″ W	70°11′39″ W	70°24′15″ W	–
Altitude	2280 m a.s.l.	2300 m a.s.l.	3050 m a.s.l.	2640 m a.s.l.	–
Closest distance to LST	0.55 km	1.15 km	15.7 km	10.3 km	–
Closest distance to MST	0.26 km	0.82 km	15.1 km	9.7 km	–
Closest distance to SST	–	–	14.6 km	9.3 km	–
Altitude difference to LST	55 m	75 m	910 m	500 m	–
Altitude difference to MST	50 m	40 m	900 m	480 m	only for closest MST
Altitude difference to SST	–	–	870 m	450 m	only for closest SST

telescopes in each hemisphere and the planned close-by LGS facilities. In Section 5, we discuss the results and conclude. There follow some appendices for the derivation of several larger formulae.

2 COMPUTATION OF AO-LASER INDUCED LIGHT ON NEIGHBOURING INSTALLATIONS

Throughout this section, the number of photons produced in photon detection systems of another instrument far from the LGS system is computed. Quantitative numbers are computed for the CTA, however, the formulae are kept as general as possible, and can be applied to any similar case.

The main parameters of the LGS systems of VLT, ELT, GTC, and TMT used for this study are reported in Table 1 together with their closest distance to CTA telescopes and altitude differences. Based on the experience with the 4 Laser Guide Star Facility (4LGSF) on Unit Telescope 4 (UT4) of the VLT (Vogt et al. 2017), an LGS system will be implemented on the ELT (Fusco et al. 2010), which will rely on

continuous wave lasers similar to those of the 4LGSF (according to the current design; Bonaccini Calia et al. 2010). The TMT will operate six lasers, each with a power of 22 W (16.5 W after exiting the beam transfer optics; Herriot et al. 2014). Finally, the upgrade of the GTC AO system with an LGS facility has been recently approved and the system is now entering its conceptual design phase (Reyes García-Talavera et al. 2016; Instituto de Astrofísica de Canarias 2018).

To compute the effect of the AO-laser light on the CTA camera pixels, we consider first typical scattering scenarios in the lower atmosphere, and their formulation in the framework of Rayleigh and Mie scattering (Section 2.1) and secondly, derive an equation for the amount of light imaged into one camera pixel, considering the geometry of the problem (Section 2.2). We discuss two case scenarios in a later section (Section 4.1).

2.1 Scattering of the laser light in the lower atmosphere

Light of wavelength λ and polarization angle ϕ is scattered in the atmosphere by air molecules (through Rayleigh scattering) and aerosols [through Mie scattering, or even more complicated ways if the shape of the scattering aerosols is not radially symmetric (Dubovik et al. 2006)]. In dry air, light is elastically[7] scattered by air molecules at a scattering angle θ with respect to the impinging photon direction into a solid angle with a differential cross-section $\mathrm{d}\sigma/\mathrm{d}\Omega$ (Penndorf 1957; Bucholtz 1995):

$$\frac{\mathrm{d}\sigma(\phi,\theta,\lambda)}{\mathrm{d}\Omega} = \frac{9\pi^2(n^2(\lambda)-1)^2}{\lambda^4 N_\mathrm{s}^2(n^2(\lambda)+2)^2}\left(\frac{6+3\rho}{6-7\rho}\right)\left(\frac{2+2\rho}{2+\rho}\right)\left(\sin^2(\phi)+\left(\frac{1-\rho}{1+\rho}\right)\cos^2(\phi)\cos^2(\theta)\right). \tag{1}$$

Here, N_s is the molecular concentration, $n(\lambda)$ the refractive index, and ρ the de-polarization ratio of air. Because $(n^2(\lambda)-1)/(n^2(\lambda)+2)$ is proportional to N_s, equation (1) is independent of density (as well as temperature and pressure; Bodhaine et al. 1999), and depends only on the components' mixture of air (which can be assumed constant throughout the troposphere and in time, except for the negligible contribution of CO_2). One can hence pick a reference condition for temperature and pressure (T, P), typically chosen as the US standard atmosphere ($T_\mathrm{s} = 288.15$ K and $P_\mathrm{s} = 1013.25$ mbar National Oceanic and Atmospheric Administration, National Aeronautics and Space Administration and United States Air Force 1976), which yields $N_\mathrm{s} = 2.547 \cdot 10^{25}\ \mathrm{m}^{-3}$. At $\lambda = \lambda_\mathrm{lgs}/n \approx 589.0$ nm, the AO-laser wavelength in air, the combination $(n^2-1)/(n+2)$ yields then 1.84×10^{-4} (Peck & Reeder 1972). Finally, the so-called *King factor* $(6+3\rho)/(6-7\rho)$ describes the effect of the molecular anisotropy of air and amounts to about 1.048 at 589 nm (Tomasi et al. 2005). The factors $(2+2\rho)/(2+\rho) \approx 1.01$ and $(1-\rho)/(1+\rho) \approx 0.95$ describe the *Chandrasekhar correction* (Chandrasekhar 1950; Bucholtz 1995). After multiplying with the number density of molecules at a given altitude h, we obtain the *volume scattering coefficient* β_mol $(\lambda, \theta, \phi, h$; see also Gaug 2014):

$$\begin{aligned}\beta_\mathrm{mol}(589.2\,\mathrm{nm},\theta,\phi,h) &\approx 1.0\times10^{-6}\left(0.95\cos^2(\phi)\cos^2(\theta)+\sin^2(\phi)\right)\frac{N(h)}{N_\mathrm{s}}\mathrm{m}^{-1}\,\mathrm{sr}^{-1}\\ &\approx 1.0\times10^{-6}\,\frac{0.95\cos^2(\theta)+1}{2}\,\frac{N(h)}{N_\mathrm{s}}\mathrm{m}^{-1}\,\mathrm{sr}^{-1},\end{aligned} \tag{2}$$

where *unpolarized light* or a *circularly polarized light* beam has been assumed in the second line. The scattering probability becomes radially symmetric in such a case. To estimate the dependence of $N(h)/N_\mathrm{s}$ on altitude, we use a typical atmospheric winter condition at the ORM[8] (Gaug, Font & Maggio 2017) with

$$\frac{N(h)}{N_\mathrm{s}} = f(h)\exp\left(-\frac{h}{H_\mathrm{mol}}\right), \tag{3}$$

where h is the altitude a.s.l. of the scattering point, and $H_\mathrm{mol} \approx 9.5$ km the average density scale height of the local troposphere (9.8 km for the central Summer months). The function $f(h)$ reproduces the slight modulation of density in the tropopause and the stratosphere and can be modelled with the following average correction function[9]:

$$f(h) \approx \begin{cases} 0.8845 + 0.0426\,h - 0.004\,h^2 + 6.1\times10^{-5}\,h^3 & \text{for } h < 18.4\ \mathrm{km} \\ 1.5917 - 0.061\,h + 0.667\,h^2 & \text{for } h > 18.4\ \mathrm{km} \end{cases}. \tag{4}$$

Whereas equation (2) is precise to a few per cent, the correction function equation (4) can show variations of more than 10 per cent, particularly in the tropopause.

Aerosols scatter light more efficiently than molecules and usually less isotropically, due to their larger sizes, although they are much less in number density. World-class astronomical observatories are however characterized by extremely low aerosol contamination on average. For instance, typical winter nights on La Palma show *aerosol optical thicknesses* (AOTs) of the ground layer of the order of only 0.02 at $\lambda =$ 532 nm, with extinction coefficients distributed exponentially with a scale height of around $H_\mathrm{aer} \approx 500$ m (Gaug et al. 2017), hence

$$\alpha(h_\mathrm{track}) = \alpha_{0,532\,\mathrm{nm}} \cdot \exp(-h_\mathrm{track}/H_\mathrm{aer}), \tag{5}$$

[7]Additionally, Raman scattering on nitrogen and oxygen molecules has been observed (Vogt et al. 2017), albeit with intensities more than three orders of magnitude lower than the pure elastically scattered return.
[8]The main results of this study are however unaffected by this assumption.
[9]Obtained from fits to NASA's NRLMSISE-00 density profiles (https://ccmc.gsfc.nasa.gov/modelweb/models/nrlmsise00.php).

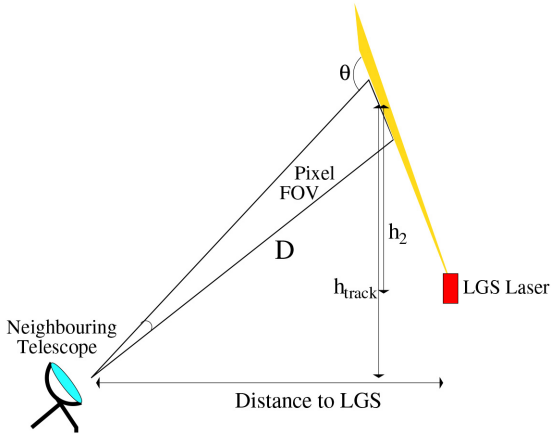

Figure 2. A sketch of the chosen geometrical conventions: The optical telescope points the LGS laser in the direction of the neighbouring telescopes, the laser light gets scattered under an angle θ towards that telescope. The scattered light travels the distance D from the scattering point to the CTA telescope mirror. The track is then observed from an altitude $h_{\rm track}$ with respect to the neighbouring telescope, and h_2 with respect to the LGS.

where $\alpha_{0,532\,\rm nm} \approx 4.5 \times 10^{-5}$ m^{-1} and $h_{\rm track}$ is the altitude of the observed part of the laser track above the neighbouring telescope. At Paranal, only the AOT has been studied so far (Patat et al. 2011), yielding similar results.

We further assume a typical Ångström index in the range from 0.5 to 1.5 for clear nights (see e.g. entries 'IZA' or 'MLO' in fig. 3 of Andrews et al. 2011), and derive $\alpha_{0,589\,\rm nm} \approx 4 \times 10^{-5}$ m^{-1} for $\lambda = 589$ nm. As we will later see, this number becomes important only on rare occasions. We can use the *Henyey–Greenstein* formula (Henyey & Greenstein 1941) to model the angular distribution of aerosol-scattered light:

$$\beta_{\rm aer}(589\,{\rm nm}, \theta, h_{\rm track}) \approx 4 \times 10^{-5} \frac{1-g^2}{4\pi} \left(\frac{1}{(1+g^2-2g\cos\theta)^{3/2}} + f \frac{3\cos^2\theta - 1}{2(1+g^2)^{3/2}} \right) \exp(-h_{\rm track}/H_{\rm aer}) \quad {\rm m}^{-1}. \tag{6}$$

Here, g represents the mean value of $\cos(\theta)$ and f the strength of a second component to the backward scattering peak. Reference values of $g \approx (0.6 \pm 0.1), f \approx (0.4 \pm 0.1)$ have been found by Louedec & Losno (2012) for a clear atmosphere and a desert-like environment in the Argentinean Andes. Contrary to the Rayleigh scattering case on molecules, the value of $\alpha_{0,\,589\rm nm}$ can show large variations, depending on both the amount of aerosols and their composition. For instance, a layer of Saharan dust (called 'calima' on La Palma) can dramatically increase the aerosol scattering cross-section (Lombardi et al. 2008). We neither take into account these nor the possibility of clouds here, because their effects are considered more important obstacles for observation by themselves than the scattered laser light. Finally, we neglected any scattering contribution from stratospheric aerosols in the Junge layer.[10]

2.2 Computation of spurious LGS light on neighbour installation's pixels

We assume that the neighbouring instrument collects light in a pixelated camera, (e.g. a CCD camera, or an array of photomultiplier tubes or silicon photomultipliers). We compute the amount of light observed by a single pixel in the camera, and assume that the telescope observes the laser uplink beam under an angle θ, such that $\theta = \pi$, if laser and the telescope's optical axis are parallel, and $\theta = \pi/2$, if the axes cross perpendicularly, see Fig. 2. The pixel observes a part of the laser track $d_{\rm track}$ across its field of view ($FOV_{\rm pix}$), at a distance D from the laser uplink beam:

$$d_{\rm track} = \frac{FOV_{\rm pix}\, D}{\sin(\theta)}\, \Omega_{\rm blur}(D), \tag{7}$$

where we have included the possibility that the laser beam width w spreads over more than one pixel:

$$\Omega_{\rm blur} = \left(1 - \exp\left(-\frac{4r^2}{w^2}\right)\right) \otimes PSF_{\perp}(r/D). \tag{8}$$

Here, $PSF_{\perp}$ is the point-spread function of the telescope, projected on to the plane perpendicular to the laser propagation and δ the angular distance from the beam axis. We can, however, assume that the LGS laser is sufficiently well collimated such that the observed beam width fits always into one camera pixel ($\Omega_{\rm blur} \approx 1$), which is the case, at least, for the CTA cameras and their neighbouring LGS stations.[11]

[10]The current stratospheric AOT amounts to 0.005, distributed over an altitude from 15 to 30 km a.s.l. Residual scattered laser light from these altitudes gets mostly focused into one camera pixel.

[11]Assuming a beam width of 0.4 m (Li et al. 2016), observed, in the absolutely worst case at 150 m (see Section 4.1) distance by an MST, yields 2.6 mrad, smaller than the MST pixel size of 3 mrad, or, at 300 m by an LST, yields 1.3 mrad, smaller than the LST pixel size of 1.7 mrad, assuming that the optical

Assuming negligible loss of laser light due to scattering out of the beam, the observed photon rate inside one laser's track can be estimated from the total laser power, $P_{\rm laser}$ (see Table 1):

$$R_{\rm ph} = \frac{P_{\rm laser}\,\lambda_{\rm laser}}{h\,c} \approx 4.9 \times 10^{19}\, N_{\rm lasers} \quad {\rm s}^{-1}, \tag{9}$$

where an individual laser power of 16.5 W has been assumed. The number of lasers simultaneously fired, $N_{\rm lasers}$, ranges from one for the case of the GTC, to four in the case of VLT, to six in the case of the TMT and the ELT.

If the distance D is large with respect to the camera dimensions (which will always be the case during observations, at least for the CTA), the scattering angle can be approximated as constant for all pixels. The light of the observed laser track scatters into a solid angle $\Omega = A_{\rm tel}/D^2$, where $A_{\rm tel}$ is the telescope's mirror area. Considering a mirror reflectivity ξ, a transmission factor $T_{\rm optics}$ for the overall optics, filters, and instrument, and a photon detection efficiency $PDE_{589\,{\rm nm}}$, the photoelectron rate, which is then amplified by the dynodes of the photomultiplier of the camera pixel, can be derived as[12]

$$R_{\rm pix} = R_{\rm ph}\, T_{\rm air}(\theta, h)\, \xi\, T_{\rm optics}\, PDE_{589\,{\rm nm}}\, \beta(\theta, h_{\rm track})\, \frac{A_{\rm tel}}{D^2}\, \frac{FOV_{\rm pix}\, D}{\sin\theta}, \tag{10}$$

where

$$\begin{aligned}\beta(\theta, h_{\rm track}) &= (\beta_{\rm mol}(589\,{\rm nm}, \theta, h_{\rm track}) + \beta_{\rm aer}(589\,{\rm nm}, \theta, h_{\rm track})) \\ &\approx \left(\frac{0.95\cos^2\theta + 1}{2}\, e^{-(h_{\rm CTA}+h_{\rm track})/H_{\rm mol}} + 1.5\left(\frac{1}{(1.13-\cos\theta)^{3/2}} + 0.17\,(3\cos^2\theta - 1)\right) e^{-h_{\rm track}/H_{\rm aer}}\right) \times 10^{-6} \quad {\rm m}^{-1},\end{aligned} \tag{11}$$

as derived in equations (2) and (6), with the average reference values for g and f inserted. Moreover, we have included an atmospheric transmission factor, $T_{\rm air}$, from the laser light dispersion point to the telescope mirror.

Besides the rather obvious observation that those cameras will be affected most that show the highest combination of the factors $T_{\rm optics}\, FOV_{\rm pix}\, A_{\rm tel}\, PDE_{589\,{\rm nm}}/D$, equation (10) requires the following comments:

(i) The distance D to the laser beam reduces the amount of registered light in a *linear* way. This is due to the combination of reduced solid angle (which scales with D^{-2}) and the increased part of the track spanned by the FOV of a pixel (which scales with D, due to the one-dimensional propagation of the laser beam).

(ii) The function $(1 + \cos^2(\theta))/\sin(\theta)$ has a (divergent) maximum at $\theta = \pi$, i.e. when the beam propagates along the telescope's optical axis. Equation (7) assumes then that the pixel integrates the light beam extending to infinite. In the case of such large scattering angles, the development of the scattering coefficient *across the FOV of the pixel* needs to be taken into account, and equation (7) translates into the geometrical overlap function of the LIDAR equation (Fernald, Herman & Reagan 1972). As a matter of fact, $(1 + \cos^2(\theta))/\sin(\theta)$ increases only by a factor of 4 at $\theta = 0.85\pi$ with respect to its minimum at $\pi/2$, which suggests that equation (10) is at least not valid for viewing angles $\theta \gtrsim 0.85\pi$.[13]

In case of observation of a same source by both the LGS-equipped and the neighbouring telescope, the photoelectron rate received by the outmost camera pixel of the neighbouring telescope can be approximated as

$$R_{\rm pix} \approx R_{\rm ph}\, T_{\rm air}(\theta, h_{\rm track})\, \xi\, T_{\rm optics}\, PDE_{589\,{\rm nm}}\, \beta(180^\circ, h_{\rm track})\, \frac{A_{\rm tel}\, FOV_{\rm pix}}{L}, \tag{12}$$

where L is the distance of the neighbouring telescope to the AO laser system (see Table 1), $\theta_{\rm lgs}$ the zenith angle of the AO-laser, and $h_{\rm track} \approx 2\,L\cos\theta_{\rm lgs}/FOV_{\rm camera}$.

Additionally to Rayleigh and Mie scattering, the telescope may observe fluorescence emission from the excited sodium layer itself. Assuming an average coupling efficiency of $(140 \div 160)$ m^2 s^{-1} W^{-1} of circularly polarized laser light at 589.159 nm to sodium atoms (Jin et al. 2014; Lu et al. 2016) and a vertical column density of sodium of $(3 \div 6) \times 10^{13}$ m^{-2} (Moussaoui et al. 2010), we can derive an average effective volume scattering coefficient of

$$\beta_{\rm Na}(\theta) \approx (1.7 \pm 0.6) \times 10^{-7}\, \left(1 + \cos^2\theta\right)\, (2.25 - 1.25\,\sin\alpha) \quad {\rm m}^{-1}, \tag{13}$$

where α denotes the angle between the laser beam propagation and the direction of the Earth's magnetic field lines. The last factor is valid if ∼10 per cent of the laser light is used to simultaneously excite the $F = 1$ hyperfine ground state of sodium with 589.157 nm wavelength ('optical pumping'; Moussaoui et al. 2008). The scattering angle dependence stems from the polarization of the laser light (Steck 2010). Equation (13) assumes a constant scattering efficiency throughout the layer, which shows in reality complicated structures (Neichel et al. 2013). Nevertheless, we will use it, together with equation (10), to roughly estimate the photoelectron rate received from the illuminated sodium layer. Our final results do not depend on the fine structure of that layer.

The concrete case of the number of spurious LGS light on CTA camera pixels will be discussed in Section 4.1.

aberrations are smaller than the size of a pixel, which is the case: Both MST and SSTs produce a point spread of about 0.02° (on-axis) to 0.05° towards the camera edges.

[12]Equation (10) has been cross-checked with an independent LIDAR return power simulation program.

[13]Note that such high scattering angles are actually possible if the laser propagates away from the neighbouring installation at maximum zenith angle. In that case, $\theta_{\rm max} \approx \pi - L/h_{\rm track} \cdot \cos^2\theta_{\rm lgs}$. However, in such cases, the scattered return flux of light is negligible, as we will see later.

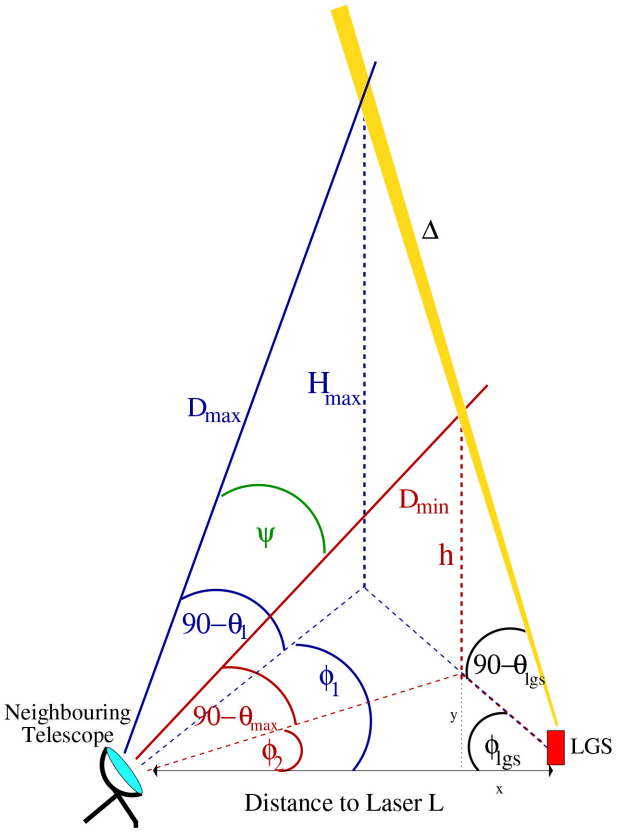

Figure 3. A sketch of the geometry to define the angle of the observability cone vetoed by the LGS.

3 PROBABILITY OF BEAM CROSSINGS

In this section, a quantitative estimation of the 'collision' probability between the LGS system and nearby telescopes is computed, together with the amount of observation time disturbed by the LGS, or even lost, for a neighbouring installation. As above, results are discussed and computed for the case of the CTA, but the used formulae are generic and can be adapted to different facilities.

We assume that an LGS impedes observation of a certain strip in the sky, if the photon rate in a series of pixels received by at least one neighbouring instrument's camera becomes larger than a maximally acceptable critical threshold $R_{\rm crit}$. We first notice that if a Laser Traffic Control System (LTCS; Summers et al. 2003) is used in its *basic configuration*[14] (see e.g. Summers et al. 2012), currently used for the ORM and the Paranal Observatory, the affected sky region can be technically avoided. Therefore, for most of the steady sources, the scheduling system can take into account the LTCS information and re-schedule a source to later times if necessary. The situation is different in case of targets that are either (a) part of multiwavelength or multiinstrument campaigns (and therefore observed with pre-defined, fixed observation times) or (b) that are the result of fast Target-of-Opportunity (ToO) alerts. The former are scheduled well in advance in coordination with other facilities and their scientific merit relies on contemporaneous data taking, while the latter are observations motivated by external triggers or other activators demanding immediate reaction and repositioning of the telescopes (such as, e.g. gamma ray burst or gravitational wave alerts or generally, flaring sources). In these cases, adequate scheduling of sources is practically impossible without a high risk of losing the science case. The frequency of such ToO alerts, the duration of their follow-up observations, and the further characteristics of the campaigns depend on the specific science case and the specificities of the neighbouring facility. Nevertheless, a general computation of the interference probability is hereafter attempted.

We start by defining the geometry of the problem in Fig. 3: an LGS is located at a horizontal distance L of an affected telescope; the LGS beam vetoes a band across the sky whose width can be assumed to be the (larger) FOV of that neighbouring instrument. This band may cross the observability cone of the close-by telescope, i.e. the region of the sky accessible by the telescope, which itself extends from zenith to the largest observable zenith angle $\theta_{\rm tel}^{\rm max}$, spanning 2π in azimuth for extra-galactic targets, or otherwise, the galactic plane, until reaching $\theta_{\rm tel}^{\rm max}$. The vetoed band starts at the point at which the laser is seen under a zenith angle $\theta_{\rm tel}^{\rm max}$ by the neighbouring instrument, at an altitude h and a distance $D_{\rm min}$. The band ends when the laser reaches a maximum altitude $H_{\rm max}$ above which the laser-induced spurious photon rates in the neighbouring instrument's cameras ($R_{\rm pix}$ from equation 10) fall below $R_{\rm crit}$. At this point, the laser beam has a distance $D_{\rm max}$ from the

[14]Basic configuration means here using a strict 'first-on-target' (or 'first-come-first-serve') policy.

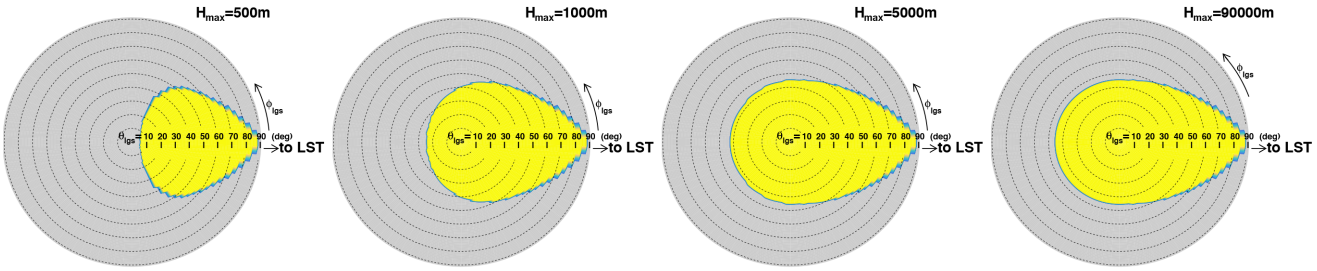

Figure 4. LGS pointings $\theta_{\rm lgs}$, $\phi_{\rm lgs}$ fulfilling condition equation (16), i.e. to enter at all the observability cone (in this case opened by a CTA-N LST), for four arbitrary values of $H_{\rm max}$. The laser is located in the centre here, the direction to the LST telescope pointing towards its right side. A maximum zenith angle of 45° has been adopted for the CTA telescope and 90° for the AO-laser, to highlight the structure of the beam crossing regions.

neighbouring telescope. The vetoed band has a length Δ and is seen from the neighbouring instrument under an angle Ψ. Using the estimation for $R_{\rm pix}$, equation (10), we can derive $H_{\rm max}$ (for details, see appendices A through C).

The condition that the LGS light enters the neighbouring instrument's observability cone at all is computed hereafter. First, we define the projected distances of the laser beam on ground:

$$\psi_x = \tan\theta_{\rm lgs}\,\cos\phi_{\rm lgs} \tag{14}$$

$$\psi_y = \tan\theta_{\rm lgs}\,|\sin\phi_{\rm lgs}|, \tag{15}$$

where $\phi_{\rm lgs}$ has been defined such that the direction towards the neighbouring instrument defines $\phi_{\rm lgs} = 0$. If multiplied with an altitude h, both yield the corresponding distances (x, y), shown in Fig. 3. The condition $\Theta(\theta_{\rm lgs}, \phi_{\rm lgs})$ that the laser light enters at all the neighbouring instrument's observability cone is then given by (see Section D for details)

$$\Theta(\theta_{\rm lgs}, \phi_{\rm lgs}) : \begin{cases} \psi_y < \tan\theta_{\rm tel}^{\rm max} & \text{for } H_{\rm max}\,\psi_x \geq L \\ \tan^2\theta_{\rm lgs} - 2\dfrac{L}{H_{\rm max}}\psi_x + \left(\dfrac{L}{H_{\rm max}}\right)^2 < \tan^2\theta_{\rm tel}^{\rm max} & \text{otherwise.} \end{cases} \tag{16}$$

Depending on the zenith and azimuth angles $(\theta_{\rm lgs}, \phi_{\rm lgs})$ of the actual LGS pointing, the vetoed band may be larger or shorter, or even null (see Fig. 4, where one can see that not all LGS pointings will be able to generate a conflict ('collision') with the neighbouring telescope, particularly if they point away from it).

For those LGS pointing directions, which fulfil condition equation (16), we can calculate the altitude h, at which the laser beam enters the observability cone of the neighbouring telescopes. After solving several geometrical relations (see again Section D), we obtain

$$h = \frac{L}{\psi_x + \sqrt{\tan^2\theta_{\rm tel}^{\rm max} - \psi_y^2}}\,. \tag{17}$$

Equation (17) defines the intersection height of the laser with the observability cone of the neighbouring instrument, and is shown as an example in Fig. 5, for the case of six TMT lasers intersecting with the observability cone of a CTA-N LST.

The angular length Ψ of the laser beam, as seen from the location of a telescope within the observability cone, from zenith to $\theta_{\rm tel}^{\rm max}$, is then

$$\cos(\Psi) = \frac{1}{2}\left\{\left(\frac{H_{\rm max}}{h}\right)^2\frac{\cos\theta_{\rm tel}^{\rm max}}{\cos\theta_1} + \left(\frac{h}{H_{\rm max}}\right)^2\frac{\cos\theta_1}{\cos\theta_{\rm tel}^{\rm max}} - \frac{\cos\theta_1\cos\theta_{\rm tel}^{\rm max}}{\cos^2\theta_{\rm lgs}}\left(1 + \left(\frac{h}{H_{\rm max}}\right)^2 - 2\frac{h}{H_{\rm max}}\right)\right\} \tag{18}$$

with

$$\frac{1}{\cos\theta_1} = \frac{1}{\cos\theta_{\rm lgs}}\sqrt{\left(\frac{L\cos\theta_{\rm lgs}}{H_{\rm max}}\right)^2 - 2\frac{L\sin\theta_{\rm lgs}\cos\theta_{\rm lgs}}{H_{\rm max}}\cos\phi_{\rm lgs} + 1}, \tag{19}$$

and h as defined in equation (17). An explicit version of equation (18), with all values inserted, is derived in the Appendix E. Fig. 6 displays Ψ as a function of the LGS pointing angles, again for the case of six TMT lasers shining into the observability cone opened by a CTA-N LST.

The part of the observable sky, which is found vetoed by an LGS laser, can then be modelled as

$$P_{\rm veto}(\theta_{\rm lgs}, \phi_{\rm lgs}) = \frac{\alpha(\theta_{\rm lgs}, \phi_{\rm lgs})\,FOV_{\rm vetoed}}{\Omega_{\rm obs}}\,, \tag{20}$$

where the total solid angle $\Omega_{\rm obs}$ available for observations by the neighbouring telescope can be computed as

(i) $\Omega_{\rm obs,extra-gal} = 2\pi\,(1 - \cos\theta_{\rm tel}^{\rm max})$ for extra-galactic targets of the neighbouring telescope.

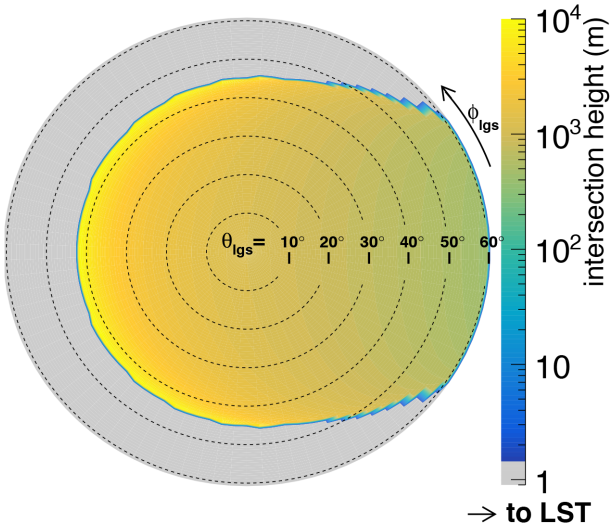

Figure 5. Polar plot of the intersection height (in metres) of the six LGS lasers of the TMT with the observability cone of an LST for fast ToO alerts in spherical coordinates $\theta_{\rm lgs}$, $\phi_{\rm lgs}$. Here, a maximum zenith angle of 60° has been adopted for the LGS. The laser is located in the centre, the direction to the LST points towards its right side. Note the logarithmic scale of the colour palette.

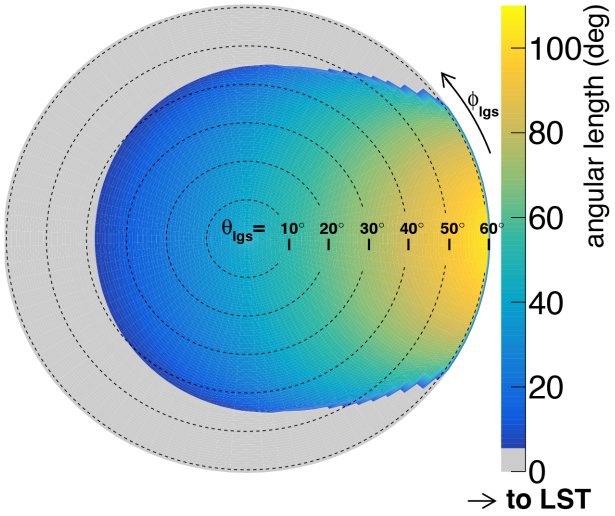

Figure 6. Angular distances Ψ (in degrees) covered by the LGS beam in polar coordinates ($\theta_{\rm lgs}$, $\phi_{\rm lgs}$), as seen from the CTA-N telescopes within its observability cone for fast ToO's (opened from $\theta_{\rm tel}^{\rm max} = 0$ to $\theta_{\rm tel}^{\rm max} = 45°$). The laser is located in the centre here, the direction to CTA-N points towards its right. A maximum possible zenith angle of $\theta_{\rm lgs} = 60°$ has been adopted.

(ii) $\Omega_{\rm obs,gal} = |b_{\rm gal}|\, 2\theta_{\rm tel}^{\rm max} \sim 0.3$ Sr for galactic observations of both the neighbouring telescopes. We assume an average diameter of the observable Milky Way $|b_{\rm gal}| \sim 0.2$ rad and that the Milky Way passes through very close to zenith.[15]

For the vetoed observation band width, we use an effective telescope field of view $FOV_{\rm tel}$, considered larger than the laser beam width, and a vetoed observation band length:

(i) $\alpha = \Psi(\theta_{\rm lgs}, \phi_{\rm lgs})$ for extra-galactic LGS pointing targets.
(ii) $\alpha = \Theta(\theta_{\rm lgs}, \phi_{\rm lgs}) \cdot b_{\rm gal}/\langle \sin\delta \rangle$ for galactic pointings of both the LGS and the neighbouring telescope, and $\langle \sin\delta \rangle \sim \sin(\pi/4)$ to account for the average tilt δ of the Milky May with the LGS beam. The condition $\Theta(\theta_{\rm lgs}, \phi_{\rm lgs})$ that the laser enters the observability cone at all is taken from equation (16).

Fig. 7 shows $P_{\rm veto}$ for the extra-galactic case and six TMT lasers shining into the observability cone of an LST.

[15]This is a reasonable assumption for the required case when both LGS and the neighbouring telescope observe a Galactic source.

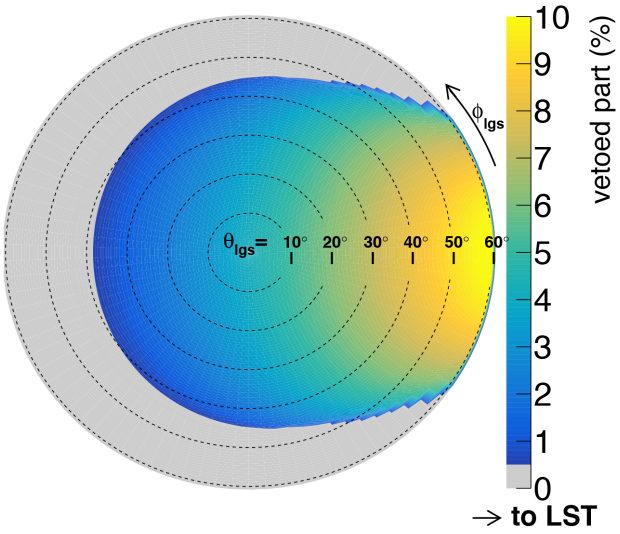

Figure 7. Part of the observability region P_{veto} (shown here in as percentage) for extra-galactic CTA-N ToO's vetoed by the LGS beam, depending on its pointing angle in spherical coordinates. Angular conventions as in the previous figures.

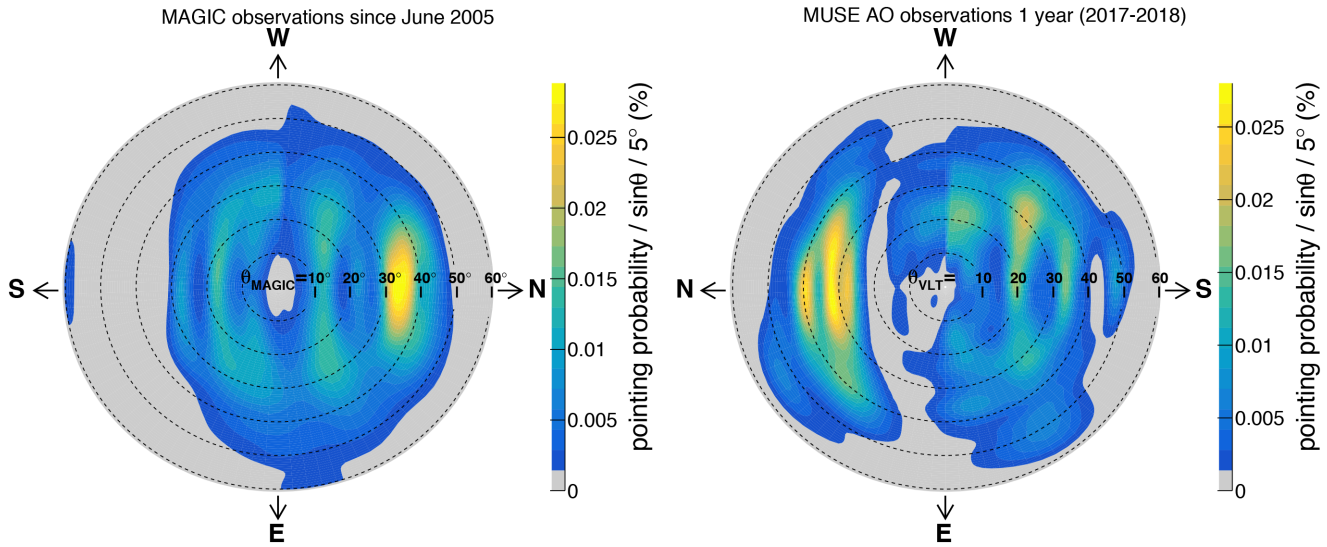

Figure 8. 10 yr of MAGIC pointing history in local spherical coordinates (θ, ϕ), smoothed and corrected for the most frequently observed calibration source and 1 yr of VLT pointing history with the MUSE instrument in Wide-Field-Mode observations, using adaptive optics.

All the previous formulae have been derived in a coordinate system where the direction from the LGS to the neighbouring telescope defines $\phi = 0$. We want to estimate the probabilities of LGS pointings in local coordinates (θ_{lgs}, $\phi_{lgs,\,orig}$), defined by $\phi_{lgs,\,orig} = 0$ when the LGS points to the north, and rotate one coordinate system to the other:

$$(\theta_{lgs}, \phi_{lgs}) = (\theta_{lgs}, \phi_{lgs,orig} - \delta_{tel}), \tag{21}$$

where δ_{tel} is the angle between the line connecting the neighbour telescopes and the LGS and the north–south axis.

Further, a probability distribution function of LGS pointings is needed: Since this is not possible to do, before an actual observation schedule is produced, we make a best guess using 10 yr of the MAGIC telescopes' (Aleksic et al. 2016) pointing history.[16] For a comparison, we also checked the local pointing field of 1 yr of GTC pointings (courtesy of Antonio Luis Cabrera Lavers) and a bit less than 1 yr of MUSE[17] Wide-Field-Mode observations carried out with adaptive optics. We find compatible results, if the different proportions of galactic and extra-galactic targets are taken into account. Varying the different pointing probability maps, the final results shown in Fig. 8 differ by

[16]MAGIC is a currently operating instrument of the same class as CTA, located at the Northern Hemisphere site of the CTA.
[17]https://www.eso.org/sci/facilities/paranal/instruments/muse/inst.html

less than 20 per cent. Since the MAGIC observations were dominated by few reference and calibration sources, we smoothed the histogram using a kernel algorithm acting on a 5 × 5 cell (McKee 1997). The outcome is shown in Fig. 8.

The pointing probability map of Fig. 8 needs to be rotated from ($\theta_{\rm lgs}$, $\phi_{\rm lgs,\,orig}$) to the local coordinate frame ($\theta_{\rm lgs}$, $\phi_{\rm lgs}$) and convoluted with the probability for laser beam vetoes:

$$P_{\rm conflict}(\theta_{\rm lgs}, \phi_{\rm lgs}) = \frac{P_{\rm veto}(\theta_{\rm lgs}, \phi_{\rm lgs})\, P_{\rm obs}(\theta_{\rm lgs}, \phi_{\rm lgs})}{\int_0^{2\pi}\int_0^{\theta_{\rm lgs}^{\rm max}} P_{\rm obs}(\theta_{\rm lgs}, \phi_{\rm lgs}) \sin\theta_{\rm lgs}\, {\rm d}\theta_{\rm lgs}{\rm d}\phi_{\rm lgs}}, \tag{22}$$

The map $P_{\rm conflict}(\theta_{\rm lgs}, \phi_{\rm lgs})$ yields the differential probability to reside in a certain pointing direction times the probability to veto the telescope pointings in that direction. Examples for the CTA-N are shown in Section 4.2.

Finally, we compute the total probability for a neighbouring telescope observation vetoed by an LGS laser by integrating equation (22) and multiplying with the duty cycle η of the LGS system:

$$P_{\rm conflict} = \eta \cdot \int_0^{2\pi}\int_0^{\theta_{\rm lgs}^{\rm max}} P_{\rm conflict}(\theta_{\rm lgs}, \phi_{\rm lgs}) \sin\theta_{\rm lgs}\, {\rm d}\theta_{\rm lgs}{\rm d}\phi_{\rm lgs}. \tag{23}$$

Here, the duty cycle of the LGS is assumed to be constant over the entire zenith angle range up to the maximum zenith angle foreseen for observations with the LGS, $\theta_{\rm lgs}^{\rm max}$.

We will apply the above formulae to a realistic case, the one of the CTA-N, in Section 4.2.

4 RESULTS

In this section, we make use of the general formulae computed in the previous section and apply them specifically to the case of the CTA. In Section 4.1, we compute the amount of LGS light scattered on to CTA camera pixels, using the formalism of Section 2, and in Section 4.2, we compute the probability of interference with the LGS lasers under best-guessed observation conditions, using the formalism of Section 3.

4.1 LGS induced light on CTA pixels

We insert a mirror reflectivity of $\xi \approx 0.85$ (assuming SiO_2 and HfO_2 coated aluminium mirrors; Pareschi et al. 2013), a camera protection window transparency of 0.92 for $T_{\rm optics}$, an altitude of $h_{\rm CTA} \approx 2200$ m for both sites, and atmospheric transmission for the air, ranging from $T_{\rm air} = 0.93^2 \approx 0.86$ to $0.97^2 \approx 0.94$ [18] for the scattered laser light[19] into equation (10) and obtain for the LGS-induced photoelectron rate on to a CTA camera pixel:

$$R_{\rm pix} \simeq (5.2 \times 10^{13}\ {\rm m}^{-1})\, N_{\rm lasers}\, PDE_{589\,{\rm nm}}\, \frac{FOV_{\rm pix}\, A_{\rm tel}}{D\ \sin(\theta)} \left(0.26\,(0.95\cos^2\theta + 1)\, e^{-h_{\rm track}/H_{\rm mol}} + \left(\frac{1}{(1.13 - \cos\theta)^{3/2}} + 0.17\,(3\cos^2\theta - 1)\right) e^{-h_{\rm track}/H_{\rm aer}}\right)\ \ {\rm s}^{-1}. \tag{24}$$

Here, $PDE_{589\,{\rm nm}}$ denotes the photon detection efficiency of the photon detector at 589.2 nm, and the relative distances between the CTA telescopes and the LGS, D, are reported in Table 1.

The CTA telescopes (LST, MST, SST) dish sizes and camera pixel fields of view, as found in Actis et al. (2011), are reported in Table 2.[20] Until very recently, photomultiplier tubes (PMTs) have been the common choice for equipping IACT cameras, due to their large PDE from 300 to 450 nm, large size, and fast time response. However, silicon photomultipliers (SiPMs) are emerging as an interesting alternative. This rapidly evolving technology has the potential to become superior to that of PMTs in terms of PDE, which would further improve the sensitivity of IACTs, and provide a price reduction per detector area. An example of a working SiPM-based IACT is FACT (Anderhub et al. 2013). In CTA, this choice is already the default for the double-mirror Schwarzschild-Couder SSTs (labelled SST-SC in Table 2) as well as the single-mirror Davies-Cotton SST (labelled SST-DC in Table 2). Schwarzschild-Couder optics demand a compact camera (Bonanno et al. 2016). However, the SiPM choice was also adopted for the SST-DC that makes use of the non-commercial Hamamatsu S10943-2832(X) (Heller et al. 2017). The MST telescopes will instead host PMT-based cameras (Glicenstein & Shayduk 2017), using the R12992-100 PMT from Hamamatsu,[21] and for the proposed Schwarzschild-Couder MST (Meagher 2014) at CTA-S. The case of LST is peculiar: its baseline

[18] From Patat et al. (fig. 3 of 2011), we obtain about 0.025 mag/airmass aerosol extinction and from Fig. 1 about 0.95 for the total molecular transmission from ground to infinity, for vertical incidence. Scaling to about 10 km above ground, this translates to 0.94 for the overall transmission at 589.2 nm. For very close scattering, molecular transmission may be negligible, yielding only $T_{\rm air} \approx 0.97$ from aerosol transmission, while larger inclination angles (hence airmass) may lead to transmissions down to 0.91 for extreme cases. Hence, for clear nights, the transmission estimate may change by up to 2 per cent, depending on the observation angle and the interaction altitude of the laser light.

[19] For the light emitted by sodium fluorescence, we use $T_{\rm air} \approx 0.85^2 = 0.72$.

[20] See also https://www.cta-observatory.org/project/technology/.

[21] http://www.hamamatsu.com/us/en/R12992-100.html

Table 2. Characteristics of the different CTA telescope types. For completeness, the PDE is not only displayed at the canonical wavelength of 589 nm, but also the pulsed Rayleigh laser systems operating at 355 and 515 nm (Rutten et al. 2006; Tokovinin et al. 2016).

Telescope	Area $A_{\rm tel}$ (m^2)	Pixel FOV $FOV_{\rm pix}$ (mrad)	Camera FOV (deg)	$PDE_{589\,\rm nm}$	PDE ($PDE_{515\,\rm nm}$)	($PDE_{355\,\rm nm}$)	LGS sensitivity $FOV_{\rm pix}\cdot A_{\rm tel}\cdot PDE_{589\,\rm nm}$ ($m^2\cdot$ rad)
LST-PMT	370	1.75	4.3	0.06 ± 0.01	0.20 ± 0.03	0.42 ± 0.03	∼0.039
LST-SiPM	370	1.75	4.3	0.28 ± †	0.37 ± †	0.3 ± †	∼0.155
MST	88	3.0	7.6	0.06 ± 0.01	0.20 ± 0.03	0.42 ± 0.03	∼0.016
SC-MST	41	1.2	7.6	0.28 ± †	0.37 ± †	0.3 ± †	$\lesssim$0.012
SST-DC	7.5	4.2	8.8	0.28 ± 0.10‡	0.32 ± 0.10‡	0.3 ± 0.05‡	$\lesssim$0.010
SST-SC	(8.0–8.3)∗	(3.0–3.5)∗	(8.3–10.5)∗	0.28 ± 0.10‡	0.32 ± 0.10‡	0.3 ± 0.05‡	$\lesssim$0.009

Notes. †The SiPM development for LST (and SC-MST) pixels is still ongoing, uncertainties can be as large as 50 per cent.
‡These cameras will probably be covered by a window coated with an optical filter which cuts out wavelengths >550 nm.
∗Actual values depend on concrete implementation.

design will make use of the PMT Hamamatsu R19200-100 (Okumura et al. 2015), with the four LSTs planned for the CTA-N already being built with PMT cameras. However, for CTA-S, as well as for a possible upgrade of the CTA-N cameras, the LST consortium is currently investigating an upgrade to SiPM (Rando et al. 2016; Arcaro et al. 2017). In such a case, the SiPM PDE at the LGS wavelength would be about four times that of the LST PMT. The LST with SiPM-equipped camera does, however, not have a technical design implementation plan, and is not yet approved. A simpler solution could be that of replacing each PMT with an array of SiPM matrices joined together; in this case, the pixel FOV will not change. Different solutions with different pixel sizes and light guides are under discussion and will not be treated here further.

Following their use in equation (10), we combine the effective telescope dish size, the pixels' field of view and their PDE into a new parameter labelled 'LGS sensitivity', shown in the last column of Table 2. One can see that the acceptance of laser track light in an LST camera pixel results to be a bit more than (or a factor of 10 higher in the case of an SiPM-based LST camera) that of an MST camera pixel. Some of the MSTs, however, approach the LGS much more than the LSTs do. Because both MST and LST will have very similar (or even the same) superbialkali photomultipliers, at least before a possible upgrade, the differences in $PDE_{589\,\rm nm}$ should be negligible between both. Values of $PDE_{589\,\rm nm} = (0.06 \pm 0.01)$ can be expected, maximally varying from 5 to 9 per cent (see e.g. Toyama et al. 2015; Mirzoyan et al. 2017). On the other hand, the SST cameras (Maccarone et al. 2017; Samarai et al. 2017), equipped with SiPM, are very sensitive at 589 nm, of the order of 30 per cent (Billotta et al. 2014; Otte et al. 2017). However, some of the current SST designs try to cover the camera with protective windows coated with an optical filter to remove wavelengths longer than 550 nm.

In order to provide reference numbers illustrating the severity of a laser beam crossing the CTA telescopes' field of view, we have selected two case scenarios. Concentrating on the relative direction of laser and telescopes, we define:

(i) A **low severity case**, expected to happen most frequently among the presented scenarios: The CTA observes at 30° zenith angle towards the south, i.e. the LGS systems at the ORM, or the north, i.e. the LGS at the ELT, whose lasers point vertically upwards, and the beams cross (see Fig. 9 left). The distance to the laser beam is then always larger than 500 m at the CTA-N, and larger than 30 km at the CTA-S. Scattering occurs then at altitudes higher than 500 m in the north, and 25 km in the south, respectively. In this case, the scattering angle is 150 deg and scattering normally dominated by molecules.

(ii) A **maximal severity case**, yielding the highest possible impact of the lasers on a CTA telescope, although this scenario is very unlikely to occur: The laser propagates at the minimally allowed elevation exactly towards the CTA, where the telescopes look into the direction of the laser, at 65° elevation (see Fig. 9 right). The distance to the laser beam is then as low as 150 m in the case of the closest MST to the GTC laser beam, observed at only 130 m altitude above the MST. Scattering occurs at altitudes ranging from 130 to 480 m for the closest MST and LST, respectively. In this case, the scattering angle is 90° and scattering of the laser light is likely dominated by aerosols.

The results of these case scenarios are quantified in Table 3. All of the studied cases focus the beam size into one camera pixel $\Omega_{\rm blur} = 1$, even in the extreme case of a maximum approach of the TMT lasers. In that case, the laser will have a width of about $w \approx 0.3$ m, observed at a distance of $D \approx 400$ m, hence $w/D < 0.8$ mrad $\ll FOV_{\rm pix}$.

As a first important outcome, we see that both in the low and maximal severity cases, the impact of either the VLT or ELT LGS is negligible in the Southern hemisphere installation: the predicted photoelectron rate is always below 0.3 p.e./ns for the cameras equipped with PMTs. This value is of the order of the p.e. rate produced by the local night sky background light, expected to produce roughly $0.3 \div 0.4$ p.e./ns (Fruck et al. 2015). Such a small effect, limited to few pixels, is properly treated in the data reconstruction. SiPM equipped SST cameras expect a night sky background rate of $\gtrsim 0.04$ p.e./ns. The LGS induced may produce an additional background rate of the same order of magnitude, however these cameras are not at all limited by such negligible backgrounds.

A different result is instead found for the Northern hemisphere installation of the CTA. The lasers from both the TMT and the GTC do have a sizeable impact on the camera images of the CTA telescopes, even in the low severity case. In order to further illustrate the results for the CTA-N, we compare the LGS-induced photoelectron rates with those expected from a star illuminating the same pixel. Fig. 9 (bottom)

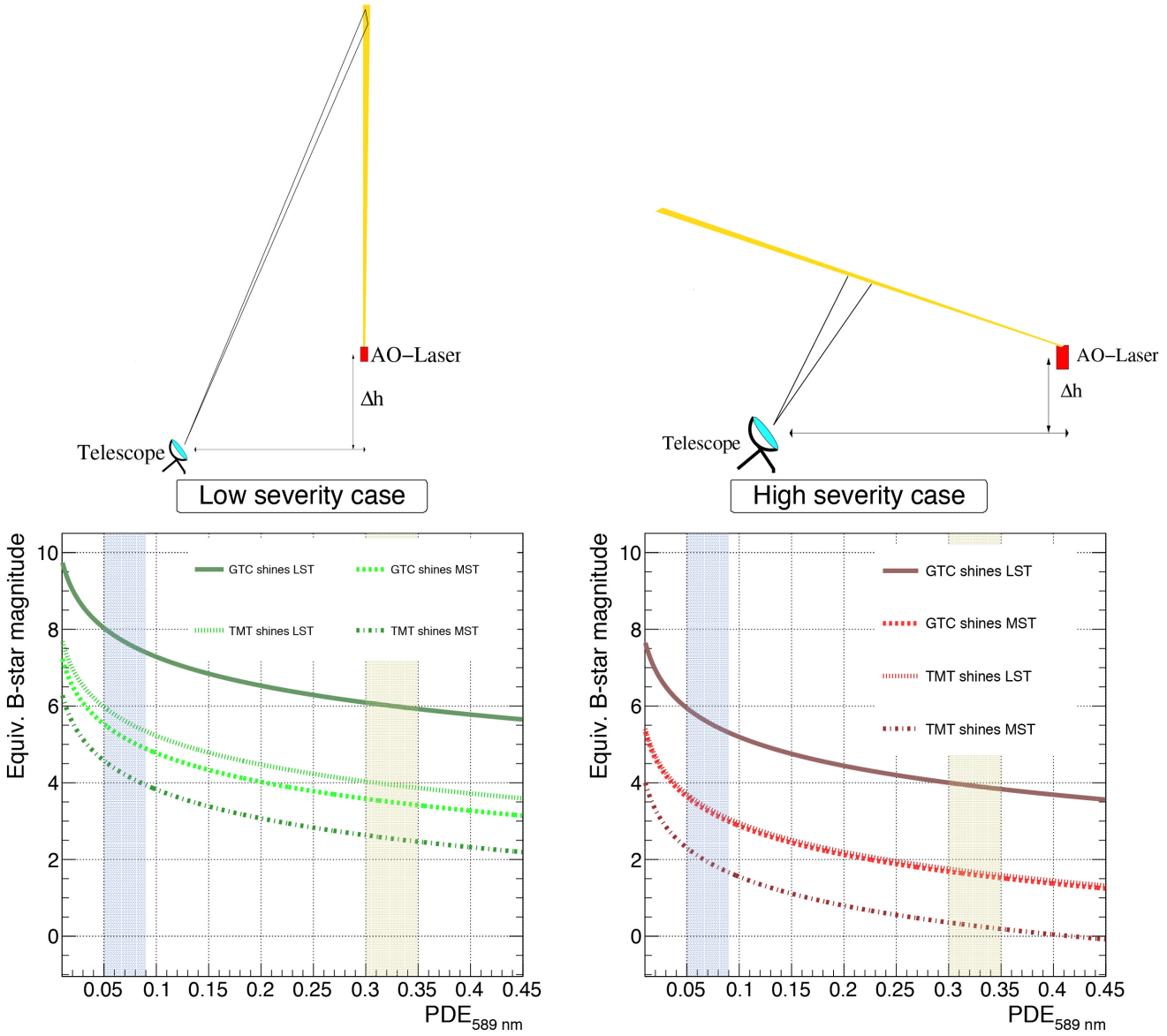

Figure 9. Left: a low severity case scenario, with the LGS laser pointing upwards, while the CTA-N observes at 45° zenith angle towards the LGS. Right: a maximal severity case scenario, with the laser pointing towards CTA-N, under the lowest allowed elevation, and CTA-N looking into the laser beam. Top: a sketch of the pointing situation, Bottom: equivalent *B*-star magnitudes for camera pixels for different PDE values at 589 nm in these case scenarios. The blue and yellow shaded areas depict the case for PMT, and SiPM-equipped cameras, respectively. The magnitudes have been derived assuming the Vega spectrum from Bohlin (2007) and a PDE at 440 nm wavelength of $\mathrm{PDE}_{440\,\mathrm{nm}} = 0.35$ and a spectral width of the PDE of $\mathrm{d}\lambda/\lambda = 0.2$. A global atmospheric extinction of $z = 0.25$ has been further assumed for the star light at *B*-filter wavelengths.

shows the equivalent *B*-star magnitudes in one pixel versus the photon sensors PDE at the LGS wavelength for the CTA-N. Two vertical bands highlight the PDE of PMT-like sensors (left blueish band) and SiPM-like sensors (right yellowish band). One can observe that the laser light may produce the same photoelectron rate as that of a *B*-star of magnitude $1^m \div 2^m$ in the maximal severity case.

If both LGS laser and CTA observe the same source, the CTA cameras will observe the Rayleigh plume from an altitude $>2D/FOV_{\mathrm{camera}}$ and fluorescence emission of the mesospheric sodium layer. In the worst case, the illuminated sodium layer will be seen by CTA under an angular length Ψ of

$$\Psi \lesssim \frac{\Delta H\, L}{H^2}\,, \tag{25}$$

where H denotes the distance to the layer centroid $H \approx 89.7$ km and ΔH is the average layer width. The resulting angular length is always smaller than one camera pixel for the CTA-N. The full layer will hence be seen as just an additional star. In the south, Ψ can become as long as 10 camera pixels, however their average flux results to be always less than 0.05 p.e./ns, even in the case of an upgraded LST camera. The photoelectron rate from the Rayleigh plume, observed by the outmost camera pixel at the CTA-N, is visible in the closest MST from greater

Table 3. Expected photoelectron fluxes in a camera pixel for the two studied severity cases.

Case	Distance to laser track (km)	Scattering altitude (km)	Flux per pixel (for N lasers) (p.e./ns)	Main scattering factor	Flux per pixel ($N = 6$) PMTs (p.e./ns)	Flux per pixel ($N = 6$) SiPMs (p.e./ns)
CTA Northern hemisphere site						
			Maximal severity			
GTC → LST	0.30	0.27	$76 \cdot PDE_{589\,nm}$	Aerosol	5	24
GTC → MST	0.15	0.13	$76 \cdot PDE_{589\,nm}$	Aerosol	5	n.a.
TMT → LST	0.53	0.48	$34 \cdot N \cdot PDE_{589\,nm}$	Molecular/Aerosol	12	65
TMT → MST	0.39	0.35	$22 \cdot N \cdot PDE_{589\,nm}$	Molecular/Aerosol	8	n.a.
			Low severity			
GTC → LST	1.10	0.95	$29 \cdot PDE_{589\,nm}$	Molecular	2	9
GTC → MST	0.52	0.45	$30 \cdot PDE_{589\,nm}$	Molecular/Aerosol	2	n.a.
TMT → LST	2.30	2.00	$12 \cdot N \cdot PDE_{589\,nm}$	Molecular	4	22
TMT → MST	1.64	1.42	$7 \cdot N \cdot PDE_{589\,nm}$	Molecular	3	n.a.
CTA Southern hemisphere site						
			Maximal severity			
ELT → LST	7.4	6.8	$0.6 \cdot N \cdot PDE_{589\,nm}$	Molecular	0.2	1.2
ELT → MST	7.2	6.5	$0.3 \cdot N \cdot PDE_{589\,nm}$	Molecular	0.1	n.a.
ELT → SST	7.0	6.3	$0.03 \cdot N \cdot PDE_{589\,nm}$	Molecular	n.a.	0.06
VLT → LST	4.8	4.4	$1.2 \cdot 4 \cdot PDE_{589\,nm}$	Molecular	0.3	1.6
VLT → MST	4.5	4.1	$0.5 \cdot 4 \cdot PDE_{589\,nm}$	Molecular	0.1	n.a.
VLT → SST	4.3	3.9	$0.07 \cdot 4 \cdot PDE_{589\,nm}$	Molecular	n.a.	0.09
			Low severity			
ELT → LST	31.4	27.2	$0.06 \cdot N \cdot PDE_{589\,nm}$	Molecular	0.02	0.1
ELT → MST	30.2	26.2	$0.03 \cdot N \cdot PDE_{589\,nm}$	Molecular	0.01	n.a.
ELT → SST	29.2	25.3	$0.004 \cdot N \cdot PDE_{589\,nm}$	Molecular	n.a.	0.007
VLT → LST	20.6	17.8	$0.2 \cdot 4 \cdot PDE_{589\,nm}$	Molecular	0.06	0.3
VLT → MST	19.4	16.8	$0.1 \cdot 4 \cdot PDE_{589\,nm}$	Molecular	0.03	n.a.
VLT → SST	18.6	16.1	$0.02 \cdot 4 \cdot PDE_{589\,nm}$	Molecular	n.a.	0.02

than $4 \div 12$ km for the GTC and TMT lasers, respectively, and the received rate is always smaller than 1.6 p.e./ns for both cases at 60° observation zenith angle and <0.9 p.e./ns for observations at zenith, using equation (12). In the absolutely worst case, the Rayleigh plume will leave spurious photoelectron rates larger than those from the typical night sky background in a line starting from the outer camera edge up to half the camera radius.

4.2 Probability of interference during CTA fast repositioning

In this section, we make use of the formalism of Section 3 to estimate the fraction of time in which the LGS will interfere with CTA operations in such a way that the underlying science case may be degraded or put at risk. Given the results from the previous section, in which we show that both the VLT and ELT LGS will have a negligible impact on CTA-S, we will focus on the CTA-N only, and particularly on the interference of the TMT LGS with the CTA telescopes. We cannot make accurate predictions of the foreseen observing programmes of the CTA-N, for the time after the TMT will start operations,[22] because most of the CTA observing time will be open for guest observer proposals. However, the CTA consortium can use 40 per cent of the first 10 yr of CTA operations in the form of proprietary key science projects. We use these to make a reasonable guess as to the distribution of target and observation types.

Some of the CTA-N's core science deals with fast transients and amounts to about 45 h/yr/site for galactic ToO's and 120 h/yr/site for extra-galactic ones for the first 12 yr of operation (see chapter 9 of The Cherenkov Telescope Array Consortium et al. 2017). We did not include open time, nor director's time, which may increase that number further. Both are however not expected to alter the previous numbers significantly. A prediction for the time reserved for 'rapid' multiwavelength campaigns with allocated and immovable time slots can be obtained from chapter 12 of The Cherenkov Telescope Array Consortium et al. (2017) summing up to 245 h yr^{-1} for the CTA-N, all dedicated to extra-galactic targets. Further assuming that CTA-N follows up each alert for an average of 2 h (which is rather standard for this

[22] Foreseeably after 2027.

Table 4. Tilts of the lines connecting an optical telescope location with a CTA-N telescope, with respect to the north–south axis.

Opt. telescope	Closest CTA-N telescope	$\delta_{\rm tel}$ (deg)
GTC	LST	0
	MST	−22
TMT	LST	22
	MST	20

technique), we can expect about 180 fast or immovable re-positionings per year, hence one fast or immovable re-positioning every one and a half nights for extra-galactic targets and one fast re-positioning every 11 nights for galactic sources.

Fast ToO observations are typically expected to happen in *normal observing mode*, i.e. making use of the typical CTA-N field of view of about 8 deg.[23] However, we may assume that such observations may be observed up to 1 deg off-axis,[24] to avoid the laser beam, hence $FOV_{\rm vetoed} \approx 6^\circ$.

To start, we set $R_{\rm crit}$ to the typical night sky background (NSB) rate for extra-galactic sources. This somewhat arbitrary criterion has been chosen assuming that the individual pixel rate control will get active, at least in the case of the LSTs, and raise the trigger thresholds of the illuminated pixels. Loss of sensitivity at the energy threshold is then expected. Later on, we will investigate in more detail the dependence of the observation time loss on $R_{\rm crit}$. The maximum altitude $H_{\rm max}$ comes out to be approximately $14 \div 20$ km above ground for the GTC laser and $18 \div 26$ km above ground for the six TMT lasers used together. If the LST camera is equipped with SiPMs, without further protecting filters, the LGS light will disturb observations up to 32 km above the ground.

We assume now a maximum zenith angle for CTA-N's rapid re-positioning targets of $\theta_{\rm tel}^{\rm max} = 45^\circ$. The extra-galactic ToO occurrence phase space covers then a solid angle of about $\Omega_{\rm ToO,\ extra\text{-}gal} \approx 1.8$ sr, and $\Omega_{\rm ToO,\ gal} \lesssim 0.3$ sr.

We apply the above occurrence estimates of fast ToO's and time slots reserved for multiwavelength campaigns, together with the distances between CTA-N telescopes and the two LGS facilities at GTC and the TMT (Table 1) and the values of $\delta_{\rm tel}$ (Table 4) to equation (22). The resulting probability maps to reside in a certain pointing direction times the probability to veto a CTA-N ToO pointing in that direction for extra-galactic observations (the so-called 'conflict probability maps') are shown in Fig. 10 (left side), for the LST case only, but are almost identical for the case of the MST. The reason for this similarity can be found in the geometry of the system: because the maximum altitudes $H_{\rm max}$ are considerably larger than the distance between LGS and CTA telescope in both cases and consequently the intersection heights h, the contribution of the visible laser path length at the highest altitudes (e.g. from 20 to 26 km) to the vetoed angular length Ψ is small. In other words, Ψ scales in zeroth order as $\mathrm{atan}(H_{\rm max}/L)$, which becomes flatter and flatter as the argument $H_{\rm max}/L$ gets larger. The vetoed pointing maps for CTA-N are hence rather insensitive to the exact values of $H_{\rm max}$ and consequently $R_{\rm crit}$. Even assuming $R_{\rm crit} = 0$ (i.e. no collision allowed at whatever level), the conflict probabilities increase by less than 5 per cent with respect to $R_{\rm crit} = 1$. In order to highlight these dependences, we show the same conflict probability maps for largely enhanced values of $R_{\rm crit}$ for the case of an LST camera equipped with PMTs (top) or with SiPMs (bottom). As expected, the SiPM equipped telescope shows higher conflict probabilities with a smaller dependence on $R_{\rm crit}$, whereas the PMT equipped camera can reduce the conflict probability by about a factor of 2, if $R_{\rm crit}$ is chosen to be 20 times larger than the typical background rate. The integral of all maps is written below on the same figures and provides the total probability to have an extra-galactic CTA-N ToO vetoed, *once the LGS is used at all*. For a comparison, we also checked the local pointing field of 1 yr of GTC pointing (courtesy of Antonio Luis Cabrera Lavers) and found compatible results. If we use instead a 1 yr VLT LGS pointing history together with the MUSE instrument, about 20 per cent lower conflict probabilities are obtained.

The integrated probabilities are finally inserted in equation (23), using the LGS duty cycles listed in Table 1. These final results are summarized in Table 5.

5 SUMMARY AND CONCLUSIONS

In this work, we have explored the effect that LGSFs, as those foreseen on several present and future large optical telescopes, such as the VLT, ELT, the GTC, and the TMT, have on neighbouring telescopes, particularly those observing with large FOVs. LGS systems operate high-power continuous wave lasers at a 589.159 nm vacuum wavelength to excite sodium nuclei in the upper mesosphere. The laser light can scatter into the FOV of the neighbouring instruments and affect data taking or reconstruction.

[23] Which is, in this case, provided by the MST cameras, while for CTA-S a larger FOV of 10 deg is obtained with the SSTs, see Table 2. The CTA provides also the possibility to observe with even larger fields of view of up to 15° in 'divergent pointing mode'. These are, however, not expected to be employed for rapid pointings, at least for the moment.

[24] The sensitivity of IACT telescopes decreases off the optical axis of the telescopes, however this happens rather slowly, as shown for the MAGIC case (Aleksic et al. 2016), and in CTA in recent simulations. The latter shows that maximally 20 per cent loss of point-source sensitivity is obtained for the case of 1 deg off-pointing, considerably reduced for medium and high gamma-ray energy ranges.

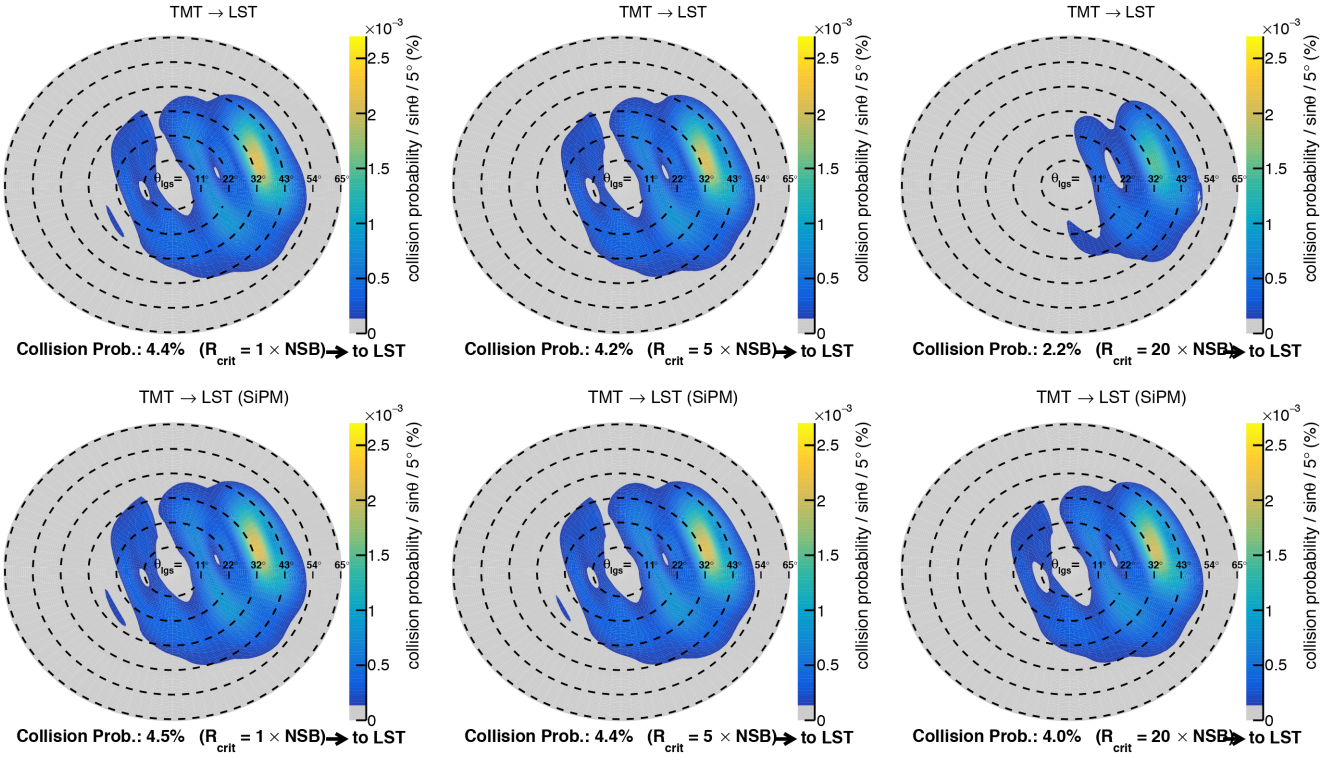

Figure 10. A probability map of conflicts of the LGS with the observability region for extra-galactic CTA-N ToO's, depending on the LGS-lasers' local pointing angles ($\theta_{\rm lgs}$, $\phi_{\rm lgs}$), obtained from a smoothed map obtained from 10 yr of MAGIC data pointing history in local zenith/azimuth coordinates (upper two figures: from 0 to 60 deg; centre and bottom figures: from 0 to 65 deg). The laser is located in the centre, the direction to the CTA-N telescope points always towards its right side, but the different pointing probabilities for the LGS (with respect to CTA-N) have been taken into account. The text on the bottom shows the total integrated probability. If instead the pointing probability map from 1 yr of GTC pointing is used, conflict probabilities about half a per cent higher are obtained.

Table 5. Probabilities of conflicts ('collisions') between LGS and CTA-N fast-ToO observations.

Optical telescope	Duty cycle LGS η (1)	Max. laser zenith angle (deg)	Prob. conflict per simult. observations (1)	Prob. conflict per ToO (1)	Estimated number of ToO's (yr^{-1})	Estimated occurrence of conflict (yr^{-1})
			Extra-galactic ToO's CTA-N			
GTC	0.15	60	0.045	0.007	180	1.2
TMT	0.75	65	0.045	0.034	180	6.1
			Galactic ToO's CTA-N			
GTC galactic	0.08	60	0.094	0.007	22	0.17
GTC extragal.	0.07	–	0.045	0.003	22	0.07
GTC total	0.15	–	–	0.008	–	0.24
TMT galactic	0.38	65	0.094	0.036	22	0.78
TMT extragal.	0.37	–	0.045	0.017	22	0.37
TMT total	0.75	–	–	0.053	–	1.05

We have computed general equations to predict the number of scattered photons into a camera pixel, as well as estimates for the fraction of time lost because of possible crossings of the neighbouring telescope FOV by the laser beam. We have later on applied those equations quantitatively to the case of the CTA, a planned ground-based array of gamma-ray instruments, currently under construction at the Observatorio del Roque de Los Muchachos, La Palma, and soon at the Armazones valley, close to Paranal, in Northern Chile. The Northern hemisphere array, CTA-N, will contain two types of telescopes, the LST and the MST, and may be affected by the GTC, and possibly the TMT LGS. In the Southern hemisphere, the CTA-S will contain three types of telescopes, adding the SST type, and is located close to the VLT and ELT LGS.

In Section 4.1, the amount of scattered laser light into CTA camera pixels has been computed, and two case scenarios, a low and a maximal severity case, studied. The obtained numbers provide a rough estimate for the ranges within which LGS-induced photoelectron rates can be expected, namely for the GTC laser: from 2 to 5 p.e./ns for PMT-based LST or MST cameras to about 10–30 p.e./ns for an LST camera equipped with SiPM; for the TMT LGS with six simultaneous beams: from 3 to 14 p.e./ns for PMT-based LST or MST cameras to about 30–80 p.e./ns for an LST camera equipped with SiPM; for the more distant VLT with four lasers or ELT lasers with six beams, rates lie always well below 1.6 p.e./ns, even in the case of an LST camera equipped with SiPM, otherwise below 0.3 p.e./ns. The SSTs, which are only deployed in the south, are not affected at all by the VLT or the ELT lasers (rates below 0.01 p.e./ns), although they approach the VLT and ELT most. The critical combination is hence the one of the TMT (in less extent the GTC) lasers shining into the CTA-N telescopes, especially if LST cameras are potentially upgraded to SiPM in the future. The obtained count rates can be compared to those of the NSB, expected to produce roughly 0.3(0.4) p.e. per MST (LST) pixel per nanosecond, respectively (Fruck et al. 2015). However, observations are also planned under partial moon light, with NSB rates up to about 20 times higher than the previous numbers, under reduced sensitivity (see e.g. Ahnen et al. 2017). The effect of all investigated cases is similar to having a row of magnitude down to as low as 1^m, *B*-stars crossing the camera. Even if the six TMT lasers are fired in a divergent mode, only one row will be seen in the telescope cameras, i.e. the different laser beams cannot be resolved.

The fluorescing sodium layer itself measures 11 km on average, and can even reach 16 km in exceptional cases (Moussaoui et al. 2010). It is however harmless if found in the FOV of the neighbouring telescope, if both installations are sufficiently close (as is the case at CTA-N). At larger distances, the layer can spread over several pixels (as at CTA-S), but the light flux received by a single camera pixel is then considerably lower than the artificial star produced in the telescope housing the LGS, and probably negligible. This is the case at CTA-S. Some residual spurious light of the order of 1 p.e./ns will be received, however, at the CTA-N by the outmost camera pixels of the closest MSTs from the Rayleigh plume of the LGS lasers of the GTC and the TMT, if both installations observe the same source.

In this situation, the laser photons are not a danger for the safety of the CTA-N cameras. Each CTA-N camera pixel is equipped with an automatic high-voltage down-regulation in case of excessive anode current, which makes observations safe. This mechanism will probably also protect the CTA-N against too high data rates of fake triggers. However, analysis of data affected by such an LGS laser beam crossing the camera is challenging and should be avoided, apart from the inevitable loss of sensitivity. Experience with the MAGIC telescopes has shown that additionally the laser beam can confuse the star-guider analysis software used to correct the pointing of the telescopes with the help of CCD cameras. Whereas solutions based on Notch filters (Schallenberg et al. 2010) exist for the CCD cameras, similar approaches for the CTA camera pixels require future study and some innovation effort: coating of curved surfaces with filters is not straightforward, nor thin filters resisting all types of weather phenomena, like temperature changes, humidity cycles, etc. to which, for instance, a protecting plexiglas of the cameras is exposed during night. Also, losses of Cherenkov photons in the wavelength range from 300 to 550 nm are an issue.

In Section 4.2, we derived the probabilities that a CTA-N observation collides with the LGS laser beam causing an unacceptably high photoelectron rate in the CTA-N camera, when different sources are observed.[25] We find around 1 per cent (3 per cent) for extra-galactic observations of CTA-N to collide with the GTC(TMT) LGS beams, and around 1 per cent (5 per cent) for galactic observations, respectively. The lower probabilities for the GTC laser are due to both its smaller relative duty cycle and its lower laser power, which in consequence allows us to cross the CTA-N field of view at a lower limiting altitude, even if CTA-N telescopes approach that laser much closer. These probabilities can be reduced by only 5 per cent, if LGS laser-induced additional p.e. rates of up to five times the natural dark NSB rate are allowed. Relieving this requirement to 20 times the NSB rate (corresponding to observations under partial moon light) reduces the conflict probabilities by about a factor of 2, unless an SiPM upgraded LST camera is used, for which the reduction is only of the order of 10 per cent.

Since both the CTA-N observatory and the GTC/TMT LGS facilities will be included in the laser tracking control system (LTCS) of the ORM, most conflicts can be avoided by adequate scheduling of the sources. Due to the nature of the current 'basic' configuration of LTCS at the ORM, which currently follows a strict 'first-on-target' policy, this is however not the case for fast ToO alerts of CTA-N, which cannot be scheduled to later times without putting at risk the science case.

Such fast ToO's, and those requiring simultaneous multiwavelength or multimessenger coverage, will occur 180 (22) times per year for extra-galactic (galactic) targets, following the key science programmes of the CTA-N (The Cherenkov Telescope Array Consortium et al. 2017). A collision in such a case will then happen $1 \div 6$ times a year for extra-galactic ToO's with the GTC/TMT LGS beam, respectively, and $0.2 \div 1$ times a year for galactic ToO's, excluding those cases where both installations observe the same target, because the glowing sodium layer will be imaged either into one camera pixel (in the case of CTA-N) and hence treated as just an additional star, or become too faint and indistinguishable from the NSB (in the case of CTA-S). In order to minimize the impact of science loss, both for the CTA and for the GTC/TMT, we suggest a modification of the strict 'first-on-target' policy of the current configuration of the LTCS. Such 'enhanced' versions of the LTCS (Santos et al. 2016) are already operative at Mauna Kea and Paranal, but require a previous consensus on newly defined priorities for observation targeting. Assuming that the relation of time reserved for fast ToO's and multiwavelength/multimessenger observations with respect to the total available time is similar to the one foreseen for the CTA-N, we expect then a reduction of the number of conflicts leading to science loss at one or the other side by at least a factor of 3. This would include new rules such that the observation of a science target

[25]The corresponding code to produce the figures, written in *ROOT*, is available on demand.

with less urgency by one part yields priority to the other unless the levels of urgency are comparable. Such low conflict rates can then be considered negligible, if compared to other, external, disturbances, like technical problems or the weather.

ACKNOWLEDGEMENTS

The authors thank the anonymous referees for their fruitful and professional comments that helped to improve the paper. This work has been funded by the grant FPA2015-69210-C6-6-R of the Spanish MINECO/FEDER, EU. The CTA consortium gratefully acknowledges financial support from the agencies and organizations listed at https://www.cta-observatory.org/consortium_acknowledgments. This paper has gone through an internal review by the CTA consortium.

REFERENCES

Actis M. et al., 2011, Exp. Astron., 32, 193
Ageorges N., Hubin N., 2000, A&AS, 144, 533
Ahnen M. L. et al., 2017, Astropart. Phys., 94, 29
Aleksic J. et al., 2016, Astropart. Phys., 72, 76
Anderhub H. et al., 2013, J. Instrum., 8, P06008
Andrews E. et al., 2011, Atmos. Res., 102, 365
Arcaro C. et al., 2017, in 9th International Workshop on Ring Imaging Cherenkov Detectors (RICH 2016) Bled, Slovenia, September 5–9, 2016. Nucl. Instr. Methods, A876, 26
Archambault S. et al., 2017, Astropart. Phys., 91, 34
Billotta S. et al., 2014, in Andrew D. H., James B., eds, Proc. SPIE Conf. Ser. Vol. 9154, High Energy, Optical, and Infrared Detectors for Astronomy VI. SPIE, Bellingham, p. 91541R
Bodhaine B. A., Wood N. B., Dutton E. G., Slusser J. R., 1999, J. Atmos. Ocean. Technol., 16, 1854
Bohlin R. C., 2007, in Sterken C., ed., ASP Conf. Ser. Vol. 364, The Future of Photometric, Spectrophotometric and Polarimetric Standardization. Astron. Soc. Pac., San Francisco, p. 315
Bonaccini Calia D., Feng Y., Hackenberg W., Holzlöhner R., Taylor L., Lewis S., 2010, The Messenger, 139
Bonaccini Calia D., Hackenberg W., Holzlöhner R., Lewis S., Pfrommer T., 2014, Adv. Opt. Technol., 3, 345
Bonanno A. et al., 2016, Nucl. Instrum. Methods Phys. Res. A, 806, 383
Boyer C., Ellerbroek B., Gilles L., Wang L., 2010, Proceedings of 1st AO4ELT conference - Adaptive Optics for Extremely Large Telescopes. EDP Sciences, 04004, p. 6
Bucholtz A., 1995, Appl. Opt., 34, 2765
Chandrasekhar S., 1950, Radiative Transfer. Oxford Univ. Press, Oxford, UK
d'Orgeville C., Fetzer G. J., 2016, in Enrico M., Laird M. C., Jean-Pierre V., eds, Proc. SPIE Conf. Ser. Vol. 9909, Adaptive Optics Systems V. SPIE, Bellingham, p. 99090R
Dubovik O. et al., 2006, J. Geophys. Res., 111, D11208
Feng L. et al., 2016, Res. Astron. Astrophys., 16, 144
Fernald F. G., Herman B. M., Reagan J. A., 1972, J. Appl. Meteorol., 11, 482
Foy R., Labeyrie A., 1985, A&A, 152, L29
Fruck C. et al., 2015, J. Instrum., 10, P04012
Fusco T. et al., 2010, Proc. SPIE Conf. Ser. Vol. 7736, Adaptive Optics Systems II. SPIE, p. 77360D
Gaug M., 2014, J. Instrum., 9, P07026
Gaug M., Font L., Maggio C., 2017, Eur. Phys. J. Web Conf., 144, 01010
Glicenstein J. F., Shayduk M., 2017, AIP Conf. Proc., 1792, 080009
Heller M. et al., 2017, Eur. Phys. J. Web Conf., C77, 47
Henyey L. G., Greenstein J. L., 1941, ApJ, 93, 70
Herriot G. et al., 2014, Proc. SPIE Conf. Ser. Vol. 9148, Adaptive Optics Systems IV. SPIE, p. 914810
Holzlöhner R., Rochester S. M., Bonaccini Calia D., Budker D., Higbie J. M., Hackenberg W., 2010, A&A, 510, A20
Instituto de Astrofísica de Canarias, 2018, Technological Development Projects - LGS extension, http://www.iac.es/proyectos.php?op1=7&op2=18&id=10&lang=en#LGS
Jin K. et al., 2014, in Marchetti E., Close L. M., Veran J. P., eds, Proc. SPIE Conf. Ser. Vol. 9148, Astronomical Telescopes + Instrumentation IV. SPIE, Bellingham, p. 91483L
Li M. et al., 2016, in Marchetti E., Close L. M., Veran J. P., eds, Proc. SPIE Conf. Ser. Vol. 9909, Cdaptive Optics Systems V. SPIE, Bellingham, p. 99095Q
Lombardi G., Zitelli V., Ortolani S., Pedani M., Ghedina A., 2008, A&A, 483, 651
Louedec K., Losno R., 2012, Eur. Phys J. Plus, 127, 97
Maccarone M. C. et al., 2017, Proc. Sci., SISSA, Trieste, Pos(ICR2017)855
McKee D., 1997, TH2:Smooth, https://root.cern.ch/root/html534/TH2.html#TH2:Smooth
Meagher K. J., 2014, in Stepp L. M., Gilmozzi R., Hall H. J., eds, Proc. SPIE Conf. Ser. Vol. 9145, Ground-based and Airborne Telescopes V. SPIE, p. 914533
Mirzoyan R. et al., 2017, Nucl. Instrum. Methods Phys. Res. A, 845, 603
Moussaoui N., Holzlöhner R., Hackenberg W., Bonaccini Calia D., 2009, A&A, 501, 793
Moussaoui N., Clemesha B. R., Holzlöhner R., Simonich D. M., Bonaccini Calia D., Hackenberg W., Batista P. P., 2010, A&A, 511, A31
National Oceanic and Atmospheric Administration National Aeronautics and Space Administration United States Air Force, 1976, U.S. Standard Atmosphere. NOAA Document S/T Vol. 76-1562. U.S. Government Printing Office, Washington, D.C.
Neichel B., D'Orgeville C., Callingham J., Rigaut F., Winge C., Trancho G., 2013, MNRAS, 429, 3522
Okumura A., Ono S., Tanaka S., Hayashida M., Katagiri H., Yoshida T., 2016, in Proceedings of the 34th International Cosmic Ray Conference. Pos ICRC(2015), The Netherlands, p. 952

Otte A. N., Garcia D., Nguyen T., Purushotham D., 2017, Nucl. Instrum. Methods Phys. Res. A, 846, 106
Pareschi G. et al., 2013, in O'Dell S. L., Pareschi G., eds, Proc. SPIE Conf. Ser. Vol. 8861, Optics for EUV, X-Ray and Gamma-Ray Astronomy VI. SPIE, p. 886103
Patat F. et al., 2011, A&A, 527, A91
Peck E. R., Reeder K., 1972, J. Opt. Soc. Am., 62, 958
Penndorf R., 1957, J. Opt. Soc. Am., 47, 176
Rabien S. et al., 2011, in Second International Conference on Adaptive Optics for Extremely Large Telescopes, Victoria 25-30 Sept., ARGOS - The Laser Star Adaptive Optics for LBT, p. 51
Rando R. et al., 2016, in Proceedings of the 34th International Cosmic Ray Conference. Pos ICRC(2015), The Hague, Netherlands, p. 940
Reyes García-Talavera M., et al., 2016, in Marchetti E., Close L. M., Veran J. P., eds, Proc. SPIE Conf. Ser. Vol. 9909, SPIE Astronomical Telescopes + Instrumentation. SPIE, Bellingham, p. 99091C
Rutten R. et al., 2006, New Astron. Rev., 49, 632
Samarai I. A. et al., 2017, Proc. Sci., SISSA, Trieste, PoS(ICRC2017)758
Santos P. et al., 2016, in Alison B. P., Robert L. S., Chris R. B., eds, Proc. SPIE Conf. Ser. Vol. 9910, Observatory Operations: Strategies, Processes, and Systems VI. SPIE, Bellingham, p. 991024
Schallenberg U., Ploss B., Lappschies M., Jakobs S., 2010, in Atad-Ettedgui E., Lemke D., eds, Proc. SPIE Conf. Ser. Vol. 7739, Modern Technologies in Space- and Ground-based Telescopes and Instrumentation. SPIE, p. 77391X
Steck D. A., 2010, Sodium D Line Data, (revision 2.1.4, 23 dec. 2010). Available at: http://steck.us/alkalidata
Summers D. et al., 2003, in Wizinowich P. L., Bonaccini D., eds, Proc. SPIE Conf. Ser. Vol. 4839, Adaptive Optical System Technologies II. SPIE, Bellingham, p. 440
Summers D., Abrams D. C., Skvarč J., Amico P., Kuntschner H., 2012, in Brent L. E., Enrico M., Jean-Pierre V., eds, Proc. SPIE Conf. Ser. Vol. 8447, Adaptive Optics Systems III. SPIE, Bellingham, p. 84474S
The Cherenkov Telescope Array Consortium et al., 2017, preprint (arXiv:1709.07997)
Tokovinin A., Cantarutti R., Tighe R., Schurter P., Martinez M., Thomas S., van der Bliek N., 2016, PASP, 128, 125003
Tomasi C., Vitale V., Petkov B., Lupi A., Cacciari A., 2005, Appl. Opt., 44, 3320
Toyama T. et al., 2015, Nucl. Instrum. Methods Phys. Res. Sect. A, 787, 280
Vogt F. et al., 2017, Phys. Rev. X, 7, 1
Wei K. et al., 2012, in Ellerbroek B. L. , Marchetti E., Veran J. P., eds, Proc. SPIE Conf. Ser. Vol. 8447, Adaptive Optics Systems III. SPIE, Bellingham, p. 84471R

APPENDIX A: DERIVATION OF DISTANCE TO THE LASER BEAM

We define the following auxiliary variables:

$$\psi_x = \tan\theta_{\rm lgs}\,\cos\phi_{\rm lgs}, \tag{A1}$$
$$\psi_y = \tan\theta_{\rm lgs}\,\sin\phi_{\rm lgs}, \tag{A2}$$
$$\zeta_x = \sin\theta_{\rm lgs}\,\cos\phi_{\rm lgs}, \tag{A3}$$
$$A = L\,\cos\theta_{\rm lgs}/H, \tag{A4}$$

where $H\cdot\psi_x$ yields x and $H\cdot\psi_y$ yields y, and the laser length multiplied with ξ_x yields x, and will later make use of the relations:

$$\psi_x^2+\psi_y^2 = \tan^2\theta_{\rm lgs}, \tag{A5}$$
$$1+\psi_x^2+\psi_y^2 = 1/\cos^2\theta_{\rm lgs}. \tag{A6}$$

Applying Pythagoras' theorem on the three triangles contained between the AO-laser, the CTA telescope, and the projected beam intersection point on ground, we obtain

$$L_l^2 = H^2/\cos^2\theta_{\rm lgs}, \tag{A7}$$
$$L_t^2 = H^2+l_t^2\,, = H^2+(L-H\psi_x)^2+H^2\psi_y^2, \tag{A8}$$
$$= H^2/\cos^2\theta_{\rm lgs}\,\left(1+A^2-2A\zeta_x\right), \tag{A9}$$

where equation (A6) has been used in the last step, and L_t and L_l denote the distances from the CTA telescope, or the AO-laser, to the beam intersection point, and l_t and l_l the distances to the projected beam intersection point on ground, respectively.

APPENDIX B: DERIVATION OF THE SCATTERING ANGLE

We apply the cosine rule to obtain the scattering angle ϑ:

$$\cos(\pi-\vartheta) = \frac{L_t^2+L_l^2-L^2}{2L_tL_l}\,, \tag{B1}$$
$$= \frac{1-A\zeta_x}{\sqrt{1+A^2-2A\zeta_x}} \tag{B2}$$

and obtain

$$\begin{aligned}
\cos(\pi - \vartheta) &= \frac{1 - A\,\zeta_x}{\sqrt{1 + A^2 - 2A\zeta_x}}\,,\\
\cos^2\vartheta &= \frac{1 + (A\zeta_x)^2 - 2A\zeta_x}{1 + A^2 - 2A\zeta_x}\,,\\
1 + \cos^2\vartheta &= \frac{2 + A^2\,(1 + \zeta_x^2) - 4A\zeta_x}{1 + A^2 - 2A\zeta_x}\,,\\
\sin^2\vartheta &= 1 - \cos^2\vartheta = \frac{A^2\,(1 - \zeta_x^2)}{1 + A^2 - 2A\zeta_x}\,,\\
\sin\vartheta\; L_t &= A\,\sqrt{1 - \zeta_x^2}\,H/\cos\theta_{\rm lgs},\\
\sin\vartheta\; L_t &= L\,\sqrt{1 - \zeta_x^2}
\end{aligned} \tag{B3}$$

and for the combination of parameters relevant for equation (10):

$$\begin{aligned}
(1 + \cos^2\vartheta)/(\sin\vartheta\; L_t) &= \frac{2 + A^2\,(1 + \zeta_x^2) - 4A\zeta_x}{L\,\sqrt{1 - \zeta_x^2}\,(1 + A^2 - 2A\zeta_x)}\,,\\
&= \frac{2\,(1 + A^2 - 2A\zeta_x) - A^2\,(1 - \zeta_x^2)}{L\,\sqrt{1 - \zeta_x^2}\,(1 + A^2 - 2A\zeta_x)}\,,\\
&= \frac{2}{L\,\sqrt{1 - \zeta_x^2}} - \frac{A^2\,\sqrt{1 - \zeta_x^2}}{L\,(1 + A^2 - 2A\zeta_x)}\,.
\end{aligned} \tag{B4}$$

APPENDIX C: DERIVATION OF THE CRITICAL ALTITUDE

We assume molecular scattering only, and a critical photoelectron rate $R_{\rm crit}$, above which observations are deteriorated. The condition $R_{\rm pix} < R_{\rm crit}$ yields then a condition for $H_{\rm max}$, if the laser points to the direction $(\theta_{\rm lgs}, \phi_{\rm lgs})$.

Using equations (10) and (B4), we obtain

$$\begin{aligned}
R_{\rm crit} > (1.4 \times 10^{13}\ {\rm m^{-1}\,s^{-1}}) \cdot N_{\rm lasers}\,{\rm PDE}_{589\,{\rm nm}}\,{\rm FOV}_{\rm pix}\,A_{\rm tel}\,\cdot\\
\cdot e^{-H_{\rm max}/H_{\rm mol}}\left(\frac{2}{L\,\sqrt{1 - \zeta_x^2}} - \frac{L\cos^2\theta_{\rm lgs}\,\sqrt{1 - \zeta_x^2}}{H_{\rm max}^2 + L^2\cos^2\theta_{\rm lgs} - 2L\,H_{\rm max}\cos\theta_{\rm lgs}\zeta_x)}\right).
\end{aligned} \tag{C1}$$

Setting both sides equal, equation (C1) can be solved numerically for $H_{\rm max}$ using a given combination of $(\theta_{\rm lgs}, \phi_{\rm lgs})$. Fig. C1 shows an example of the critical altitude as a function of the pointing coordinates $(\theta_{\rm lgs}, \phi_{\rm lgs})$ of the GTC and the TMT laser and Fig. C2 as a function of $R_{\rm crit}$ for the case of a vertically upward pointing LGS, observed by an LST.

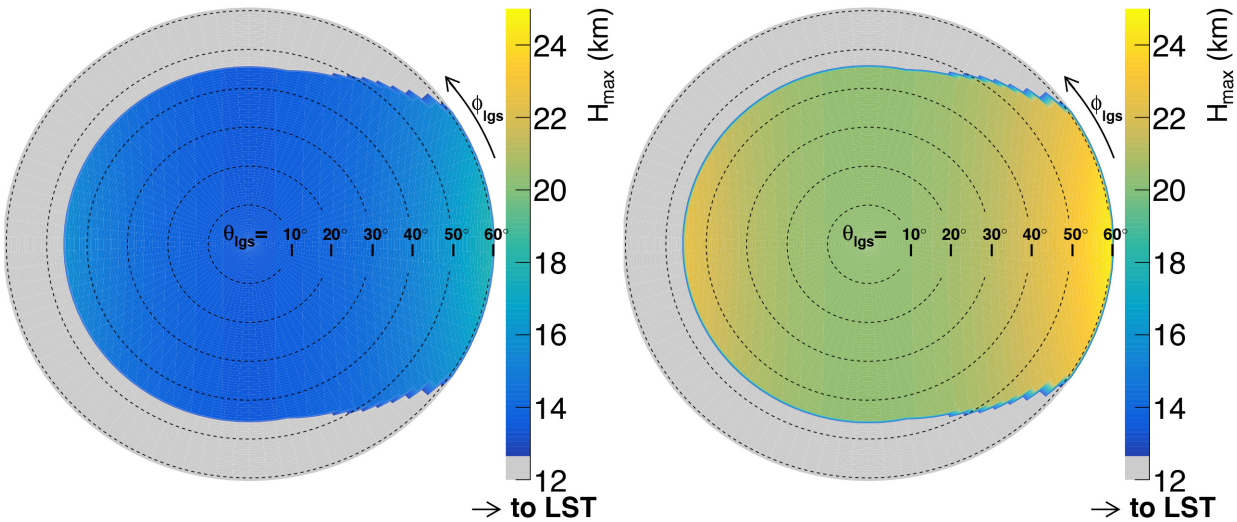

Figure C1. Polar plot of the critical altitude for the case of the GTC (left) and the TMT (right) laser shining into the observability cone of an LST. The laser is located in the centre, the direction to the LST points towards its right side.

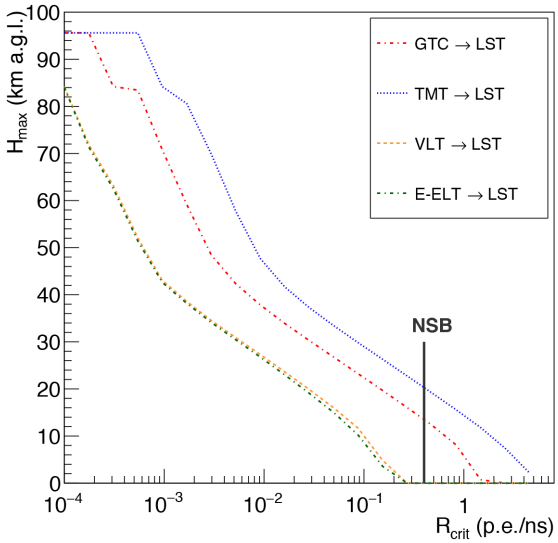

Figure C2. Critical altitude $H_{\rm max}$ as a function of the critical pixel rate $R_{\rm crit}$ for the four investigated LGS systems pointing vertically upwards.

APPENDIX D: DERIVATION OF THE OBSERVABILITY CONDITION AND HEIGHT OF INTERSECTION POINT

We apply Pythagoras' theorem on the triangle contained between the CTA telescope, the projected beam intersection point on ground, and the line connecting the distance between CTA telescope and AO-laser with the intersection point:

$$\begin{aligned} h^2 \tan^2\theta_{\rm CTA} &= y^2 + (L-x)^2, \\ &= h^2\,\psi_y^2 + (L - h\,\psi_x)^2, \\ &= h^2\,\tan^2\theta_{\rm lgs} - 2\,L\,h\,\psi_x + L^2. \end{aligned} \tag{D1}$$

Requiring that $\theta_{\rm CTA} < \theta_{\rm tel}^{\rm max}$ cannot be larger than a certain maximum zenith angle, and $h < H_{\rm max}$, we obtain

$$\tan^2\theta_{\rm lgs} - 2\frac{L}{H_{\rm max}}\psi_x + \left(\frac{L}{H_{\rm max}}\right)^2 < \tan^2\theta_{\rm tel}^{\rm max}. \tag{D2}$$

Note that equation (D2) is also valid for the cases $\psi_x < 0$ and $H_{\rm max}\,\psi_y > L$.

Now, we solve equation (D1) for h:

$$\begin{aligned} \tan^2\theta_{\rm tel}^{\rm max} &= \tan^2\theta_{\rm lgs} - 2\frac{L}{h}\psi_x + \left(\frac{L}{h}\right)^2 = \left(\frac{L}{h} - \psi_x\right)^2 + \psi_y^2, \\ h &= \frac{L}{\psi_x + \sqrt{\tan^2\theta_{\rm tel}^{\rm max} - \psi_y^2}}. \end{aligned} \tag{D3}$$

APPENDIX E: DERIVATION OF THE ANGULAR LENGTH Ψ

We define, as previously:

$$A = L\,\cos\theta_{\rm lgs}/H_{\rm max}, \tag{E1}$$

$$B = \psi_x + \sqrt{\tan^2\theta_{\rm tel}^{\rm max} - \psi_y^2}\,. \tag{E2}$$

Applying the cosine rule for Ψ, we obtain:

$$\cos(\Psi) = \frac{D_{\rm max}^2 + D_{\rm min}^2 - D^2}{2D_{\rm max}D_{\rm min}}. \tag{E3}$$

Following the relations:

$$\begin{aligned} D_{\rm max} &= \frac{H_{\rm max}}{\cos\theta_1}, \\ D_{\rm min} &= \frac{h}{\cos\theta_{\rm tel}^{\rm max}} = \frac{L}{B\cos\theta_{\rm tel}^{\rm max}}, \\ \Delta &= \frac{H_{\rm max} - h}{\cos\theta_{\rm lgs}} = \frac{1}{\cos\theta_{\rm lgs}}\left(H_{\rm max} - \frac{L}{B}\right), \end{aligned} \tag{E4}$$

we obtain

$$\cos(\Psi) = \frac{1}{2}\left\{ \frac{H_{\max}}{h}\,\frac{\cos\theta_{\rm tel}^{\max}}{\cos\theta_1} + \frac{h}{H_{\max}}\,\frac{\cos\theta_1}{\cos\theta_{\rm tel}^{\max}} - \frac{\cos\theta_1\cos\theta_{\rm tel}^{\max}}{\cos^2\theta_{\rm lgs}}\left(\frac{h}{H_{\max}} + \frac{H_{\max}}{h} - 2\right)\right\} \tag{E5}$$

with

$$\frac{1}{\cos_1^2} = \frac{1}{\cos^2\theta_{\rm lgs}} - 2\frac{L}{H_{\max}}\psi_x + \left(\frac{L}{H_{\max}}\right)^2,$$

$$\frac{1}{\cos_1} = \frac{1}{\cos\theta_{\rm lgs}}\sqrt{1 + A^2 - 2A\zeta_x}, \tag{E6}$$

$$\frac{H_{\max}}{h} = \frac{H_{\max}}{L}\,B, \quad \text{with } \mathrm{H_{max}} \text{ obtained from equation (C1)}, \tag{E7}$$

where the latter can be easily derived from equation (D1).

$$\cos(\Psi) = \frac{1}{2}\,\frac{B\,\cos\theta_{\rm tel}^{\max}\,(1 + A^2 - 2A\zeta_x) + A^2/(B\,\cos\theta_{\rm tel}^{\max}) - \cos\theta_{\rm tel}^{\max}/B\,(B - A/\cos\theta_{\rm lgs})^2}{A\,\sqrt{1 + A^2 - 2A\zeta_x}}, \tag{E8}$$

$$= \frac{\cos\theta_{\rm tel}^{\max}}{2}\,\frac{B\,(A - 2\zeta_x) + \frac{A}{B}\left(\frac{1}{\cos^2\theta_{\rm tel}^{\max}} - \frac{1}{\cos^2\theta_{\rm lgs}}\right) + \frac{2}{\cos\theta_{\rm lgs}}}{\sqrt{1 + A^2 - 2A\zeta_x}}. \tag{E9}$$

This paper has been typeset from a TEX/LATEX file prepared by the author.